https://doi.org/10.5194/essd-2025-14
Preprint. Discussion started: 6 February 2025

Open Access Earth System Science Data Discussions

Satellite-based Analysis of Ocean-Surface Stress across the Ice-free and Ice-covered Polar Oceans

Chao Liu[1], Lisan Yu[1]

[1]Woods Hole Oceanographic Institution, Woods Hole, MA, USA

Correspondence to: Chao Liu (chao.liu@whoi.edu)

Abstract. Ocean-surface stress is a critical driver of polar sea ice dynamics, air-sea interactions, and ocean circulation. This work provides a daily analysis of ocean-surface stress on 25-km Equal-Area Scalable Earth (EASE) Grids across the ice-free and ice-covered regions of the polar oceans (2011-2018 for Arctic, 2013-2018 for Antarctic), covering latitudes north of 60°N in the Arctic and south of 50°S in the Antarctic and Southern Ocean. Ocean-surface stress is calculated using a bulk parameterization approach that combines ocean-surface winds, ice motion vectors, and sea surface height (SSH) data from multiple satellite platforms. The analysis captures significant spatial and temporal variability in ocean-surface wind stress and the resultant wind-driven Ekman transport, while providing enhanced spatiotemporal resolution. Two sensitivity analyses are conducted to address key sources of uncertainty. The first addresses the fine-scale variability in SSH fields, which was mitigated using a 150-km Gaussian filter to smooth three-day SSH datasets and enhance compatibility with the other monthly product, followed by linear interpolation to achieve daily resolution. The second investigates uncertainty in the ice-water drag coefficient, which revealed that variations in the coefficient have a proportional influence on the computed ocean-surface stress under the tested conditions. These uncertainties are most pronounced during winter, with median values reaching 20% in the Arctic and 40% in the Southern Ocean. Validation efforts utilized Ice-Tethered Profiler velocity records, revealing moderate correlations (r = 0.6–0.8) at monthly timescales, effectively capturing low-frequency signals but with small northward biases. Satellite-derived velocity fields, including both Ekman and geostrophic components, explain 40-50% of the total variance. The unexplained variance reflects unresolved processes, such as mesoscale dynamics and other unparameterized factors. This dataset is publicly available at https://doi.org/10.5281/zenodo.14750492 (Liu & Yu, 2024).

https://doi.org/10.5194/essd-2025-14
Preprint. Discussion started: 6 February 2025

Open Access Earth System Science Data Discussions

1 Introduction

Earth's polar regions have undergone profound changes over the past decades, with sea ice playing a central role in the polar climate system. By modulating heat, momentum, and freshwater exchanges at the atmosphere-ice-ocean boundary, sea ice directly influences global climate dynamics (Meehl, 1984; Stammerjohn et al., 2012). In the Arctic, rapid sea ice decline has transitioned the region from predominantly thick, multiyear ice to thinner, more dynamic ice, with increased interannual variability (Comiso et al., 2008; Stroeve and Notz, 2018; Moore et al., 2022; Babb et al., 2022). Meanwhile, Antarctic sea ice trends have shown greater complexity, with a modest long-term increase observed until the mid-2010s, followed by a record loss in 2017 and a subsequent continued decline (Liu et al., 2004; Parkinson, 2019; Turner et al., 2022; Purich & Doddridge, 2023). These changes in sea ice extent and thickness have significant implications for polar systems and global climate feedbacks, influencing the Arctic's ability to regulate planetary heat, as well as impacting marine ecosystem, carbon cycling, nutrient distribution, and thermohaline circulation (Talley, 2013; Campbell et al., 2019).

Atmospheric circulation is a primary driver of sea ice dynamics and variability. Geostrophic winds, for instance, account for over 70% of sea ice velocity variability (Thorndike and Colony, 1982; Maeda et al., 2020), while broader climate modes, including the Arctic Oscillation, Pacific Decadal Oscillation, and Southern Annular Mode, influence ice extent and distribution (Rigor et al., 2002; Park et al., 2018; Lefebvre et al., 2004). These wind-driven processes interact with sea ice to modify ocean-surface stress, impacting Ekman dynamics and the transport of heat, salt, and nutrients (Yang, 2006, 2009; Meneghello et al., 2017). This feedback mechanism, often described as the "ice-ocean governor," plays an important role in regulating polar freshwater storage and circulation (Marshall and Speer, 2012; Abernathey et al., 2016; Ma et al., 2017).

Despite significant advancements in understanding these processes, direct measurements at the ice-ocean interface remain limited, with most data concentrated in the Arctic's Canada Basin (Smith et al., 2019; Regan et al., 2019). Satellite remote sensing has been instrumental in addressing these gaps, providing open ocean-surface wind retrievals available since 1988 (Yu & Jin, 2014a) and tracking sea ice motions since 1978 (Cavalieri et al., 1996). Recent advances in satellite altimetry further enable high-resolution monitoring of sea surface height (SSH) changes, offering new insights into mesoscale ocean dynamics (Armitage et al., 2016, 2017; Prandi et al., 2021).

Building upon the concepts developed in previous studies (Yang, 2006, 2009; Meneghello et al., 2018), this analysis utilizes recent satellite-based datasets on wind, ice motion, and SSH to analyze ocean-surface stress across both ice-free and ice-covered polar seas. Specifically, we present a daily analysis of ocean-surface stress at 25-km resolution using Equal-Area Scalable Earth (EASE) Grids from 2011 to 2018 for Arctic and 2013-2018 for Antarctic, covering latitudes north of 60°N in the Arctic and south of 50°S in the Antarctic and Southern Ocean (Figure 1).

Section 2 provides a description of the satellite datasets used and processing steps, along with the methods for calculating ocean-surface stress and Ekman circulation. Section 3 presents the time-mean patterns and variability of the derived surface stress and Ekman pumping fields. Section 4 addresses quantification of uncertainties in the analysis, including sensitivity to the ice-water drag coefficient and comparisons of with in-situ data.

https://doi.org/10.5194/essd-2025-14
Preprint. Discussion started: 6 February 2025

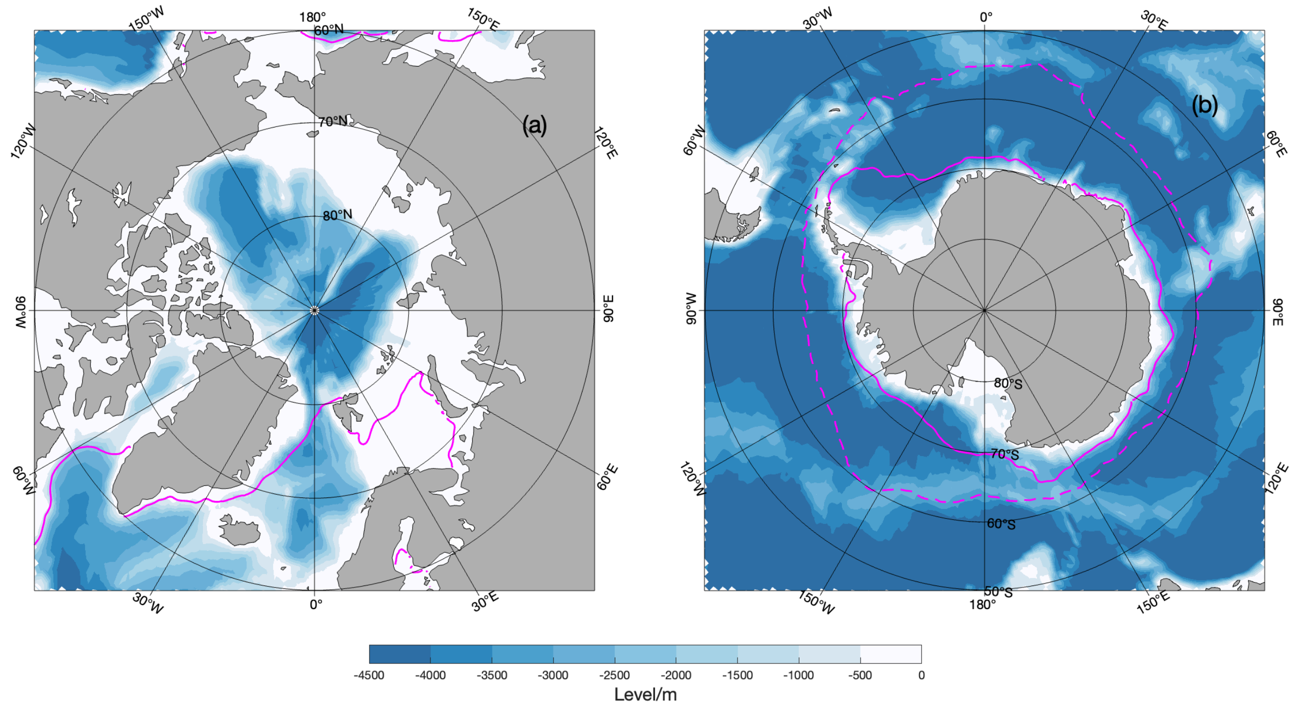

Figure 1: Study region in (a) Arctic and (b) Southern Oceans. Blue shading represents the bathymetry in meter. Solid and dashed magenta lines indicate the median sea ice extent boundaries for March and September, respectively, defined by areas with sea ice concentration.

2 Data, Method and Processing of the Analysis

2.1 Calculation of Ocean-Surface Stress and the Ekman Transport

The ocean-surface stress is estimated using the methodology proposed by Yang (2006, 2009), with modifications by Meneghello et al. (2018). The total ocean-surface stress (τ_o) is calculated as a weighted linear combination of ice–water stress (τ_{iw}) and air–water stress (τ_{aw}), based on the fractional sea ice concentration:

$$\tau_o = \alpha\tau_{iw} + (1-\alpha)\tau_{aw} \tag{1}$$

where α is set to 0 for the ice-free surfaces (defined as sea ice concentration less than 15%) and 1 for ice-covered surfaces (defined as sea ice concentration exceeding 15%). The stresses τ_{iw} and τ_{aw} are parameterized using quadratic drag laws:

$$\tau_{iw} = \rho_w C_{D,iw}\left|U_{ice} - U_e - U_g\right|\left(\boldsymbol{U_{ice}} - \boldsymbol{U_e} - \boldsymbol{U_g}\right) \tag{2}$$

and

$$\tau_{aw} = \rho_a C_{D,aw}|U_{10}|\boldsymbol{U_{10}} \tag{3}$$

where U_{ice}, U_e, U_g, and U_{10} are the local ice motion, Ekman velocity, geostrophic velocity, and equivalent neutral wind at 10-m height, respectively. ρ_w = 1027.5 kg m^{-3} and ρ_a represent the densities of water and air. In this product, τ_{aw} is taken directly from existing satellite wind products (Yu and Jin 2014a, b).

$C_{D,iw}$ is the ice-water drag coefficient and $C_{D,iw}$ = 5.5 × 10^{-3} is adopted in this product as it is a commonly recognized value. It is worth noting that, due to the limited availability of direct observations, $C_{D,iw}$ is identified as a key source of uncertainty. A sensitivity analysis is therefore provided in the following section to evaluate its potential impact.

In Equation (2), surface ocean velocity expressed as the sum of U_g and U_e. The geostrophic velocity U_g can be calculated from dynamic ocean topography datasets (McPhee 2013; Armitage et al. 2016, 2017). The Ekman velocity U_e, which moves at an angle of 45° to the right of the ocean-surface stress in the Northern Hemisphere, is calculated as:

$$U_e = \frac{\sqrt{2}e^{-i(\pi/4)}}{f\rho_w D_e}\tau_o \tag{4}$$

where f is the Coriolis parameter, and D_e is the Ekman layer depth. Since U_e and τ_o are interdependent in Eqs. (1) and (4), a modified Richardson iteration method is applied to solve them iteratively until converge is achieved, starting with $U_e = 0$ in the first iteration (Yang 2006).

Subsequently, the vertical Ekman velocity w_e can be calculated as follows:

$$w_e = \frac{1}{f\rho_w}\nabla \times \tau_o \tag{5}$$

A positive w_e indicates upwelling, while a negative w_e corresponds to downwelling.

2.2 Data Description

The calculation of total ocean-surface stress (Eqs. (1)–(4)) requires the following input datasets: ocean-surface wind stress (τ_{aw}), sea ice concentration (α), sea ice motion (U_{ice}), and dynamic topography for geostrophic velocity (U_g). A brief description of each satellite-based dataset is given in Table 1.

Table 2: Gridded satellite datasets used in the work.

Variable	Source	Resolution	Period	Reference
Surface Wind Stress τ_{aw}	OAFlux2	Daily, 0.25°	1988-present	Yu & Jin, 2014a, 2014b
Ice Motion U_{ice}	Polar Pathfinder v4	Daily, 25 km	1978-2023	Tschudi et al., 2019
Geostrophic U_g	multi-altimeter dataset	3-Day, 25 km	2011-2021 (Arctic) 2013-2021 (Antarctic)	Prandi et al., 2021

https://doi.org/10.5194/essd-2025-14
Preprint. Discussion started: 6 February 2025

Sea Ice Concentration α	NSIDC0051, v2	Daily, 25 km	1988-present	DiGirolamo et al., 2022

In this product, the air-water wind stress is taken from OAFlux2 (Yu & Jin, 2014a, 2014b), a satellite-derived 0.25-degree gridded air-sea flux daily analysis (1988 to present) developed under the auspices of NASA's Making Earth System Data Records for Use (MEaSUREs) program (Yu, 2019). OAFlux2 winds are synthesized from 19 active and passive satellite wind sensors and wind stress are calculated from the Coupled Ocean-Atmosphere Response Experiment (COARE) bulk algorithm version 3.6 (Fairall et al., 2003).

Daily sea ice motion vectors for the Arctic and Antarctic regions are obtained from the National Snow and Ice Data Center's (NSIDC) Polar Pathfinder Daily 25 km EASE-Grid Sea Ice Motion Vectors, Version 4 (Tschudi et al., 2019, 2020), covering the period from 1978 through 2023. The ice motion fields are derived from multiple sources, including passive microwave radiometers (e.g., SSM/I, AMSR-E), visible and infrared sensors (e.g., AVHRR, MODIS), scatterometers (e.g., QuikSCAT), drifting buoys (e.g., IABP), and atmospheric reanalysis winds. Feature-tracking algorithms are applied to sequential satellite images to identify ice displacement, while optimal interpolation techniques combine the various data sources to produce daily sea ice motion estimates. The resulting vectors represent sea ice displacement over a 24-hour period and are gridded onto a 25 km EASE grid.

Geostrophic velocity in the Arctic and Antarctic are obtained from the CLS/PML multi-altimeter combined Arctic/Antarctic Ocean sea level dataset (Prandi et al., 2021). This dataset spans latitudes north of 50°N on a 25 km EASE2 grid, with a temporal resolution of one grid point every 3 days. Covering the Arctic from 2011 to 2021 and the Antarctic from 2013 to 2021, the CLS dataset mitigates the spurious meridional signals often introduced by the longer sampling intervals of CryoSat-2 observations (Auger et al., 2022).

Due to the scarcity of reliable sea surface height data in polar regions, the study also uses the Dynamic Ocean Topography (DOT) dataset (2003-2021) from the Centre for Polar Observation and Modelling (CPOM; Armitage et al., 2016, 2017) for comparison and error estimate. CPOM DOT dataset offers relatively coarse spatial resolution and monthly temporal interval (Auger et al., 2022).

The Sea Ice Concentrations from Nimbus-7 SMMR and DMSP SSM/I–SSMIS Passive Microwave Data, Version 2 (NSIDC-0051, Cavalieri et al., 1996; DiGirolamo et al., 2022) is used to define the daily ice boundary based on the 15% ice concentration threshold. NSIDC-0051 provides a reliable, long-term record of sea ice concentration, making it valuable for studying sea ice conditions and large-scale climate variability (Parkinson, 2019). Widely recognized for its accuracy, the dataset is frequently used to validate and improve climate model simulations. The daily dataset is available from 1987 to the present and provide a coverage on a 25 km resolution polar stereographic grid for the both polar regions.

Another issue arises with the OAflux wind dataset, where a significant gap between its ice mask and dataset 0051 is observed after 2018 (higher than 5% of total grids). This discrepancy limits the reliability of results in the marginal zones in recent years. Therefore, considering all factors, the study period for Antarctica is constrained to six years (2013–2018), while an eight-year

https://doi.org/10.5194/essd-2025-14
Preprint. Discussion started: 6 February 2025

period (2011–2018) is maintained for the Arctic. However, updates can be easily extended as new data becomes available, particularly with the inclusion of high-resolution sea surface height measurements.

2.3 Data processing procedure

Using the methodology described in Eqs. (1)-(5) and the input data listed in Table1, the workflow for processing and analysing data to calculate ocean-surface stress and derive vertical Ekman velocity is shown in Figure 2.

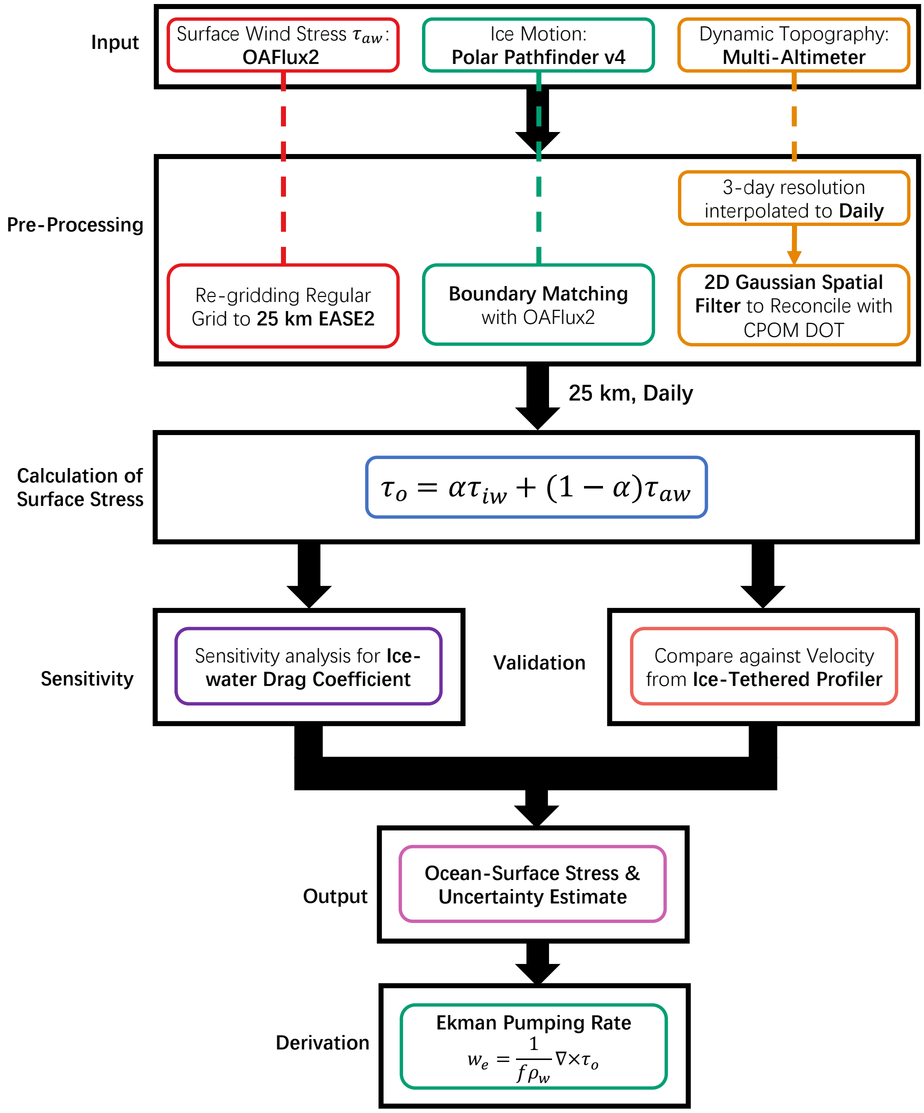

Figure 2: Workflow for data processing and analysis to calculate ocean-surface stress and derive vertical Ekman velocity.

https://doi.org/10.5194/essd-2025-14
Preprint. Discussion started: 6 February 2025

All datasets are interpolated onto a common 25 km EASE grid format, providing uniform spatial resolution and facilitating consistent analysis across the Arctic and Antarctic regions. Although the discrepancies in sea-ice boundaries are very limited over 2011-2018 (less than 2% of total grids), ice concentration and motion data are adjusted to better align with OAflux2 wind stress. Noting the 25 km resolution could introduce uncertainties near the 15% sea ice concentration boundary, which is commonly used to distinguish sea-ice cover in satellite products. In this grid, the transition between sea ice and open water can span just one grid cell. As a result, care must be taken when interpreting results in these areas to accurately capture marginal ice zone dynamics.

We employed a 2D Gaussian filter with a standard deviation of 75 km to improve consistency and interpretability between CLS and CPOM DOT datasets, which have different resolutions and small-scale characteristics. A sensitivity test is conducted to determine the optimal filter radius, ranging from 50 km to 250 km. Smaller filters (e.g., <50 km) preserve small-scale variability but may complicate the interpretation of large-scale features, while larger filters (e.g., >250 km) can excessively smooth mesoscale processes, such as boundary currents, reducing the dataset's ability to capture key processes of polar dynamics.

To find the optimal filter size, a series of tests were conducted for 2011. The effectiveness of each filter setting is evaluated using the Root Mean Squared Deviation (RMSD):

$$RMSD = \sqrt{\frac{1}{N}\sum\nolimits_{i,j}\left(w_{i,j} - w_{ref,(i,j)}\right)^2} \tag{6}$$

where w represents the local vertical Ekman velocity w_e derived from the CLS dataset, filtered with a specific Gaussian filter size (e.g., 100 km, 150 km, etc.), and w_{ref} is the reference vertical Ekman velocity calculated using the CPOM dataset. N is the total number of the grid points with sea ice coverage.

The unfiltered CLS dataset exhibits clear seasonal variations in RMSD, with values peaking at 25 cm/day during winter and decreasing in summer (Figure 3a). Applying a Gaussian filter significantly enhances agreement with the CPOM dataset, reducing RMSD by 10–15 cm/day for most of the year. However, in late summer the reduction is only 2–5 cm/day.

Increasing the filter size further enhances spatial agreement (Figure 3b). From no-filter to a 100 km filter, the annual mean RMSD is reduced to 17 cm/day, and increasing the filter size to 150 km further lowers the RMSD to 15.5 cm/day. The standard deviation of daily RMSD is also reduced by half with 150 km filter compared to the unfiltered results. However, larger filter sizes (e.g. 200 km and 250 km) yield only marginal additional improvements. Therefore, the 150 km Gaussian filter is selected as a practical and effective balance between preserving spatial features and minimizing small-scale variability for this work.

Figure 3c–h demonstrates the impact of varying filter sizes on the spatial structures of τ_o and w_e on March 15, 2011. Without filtering, the CLS dataset exhibits residual meridional striping due to satellite sampling artifacts (Auger et al., 2022). This pattern is significantly suppressed with a 150 km Gaussian filter. Between the filtered CLS-derived w_e (150 km) and CPOM-derived w_e, the correlation coefficients improving markedly from 0.77 (no filter) to over 0.95 ($p < 0.05$).

https://doi.org/10.5194/essd-2025-14
Preprint. Discussion started: 6 February 2025

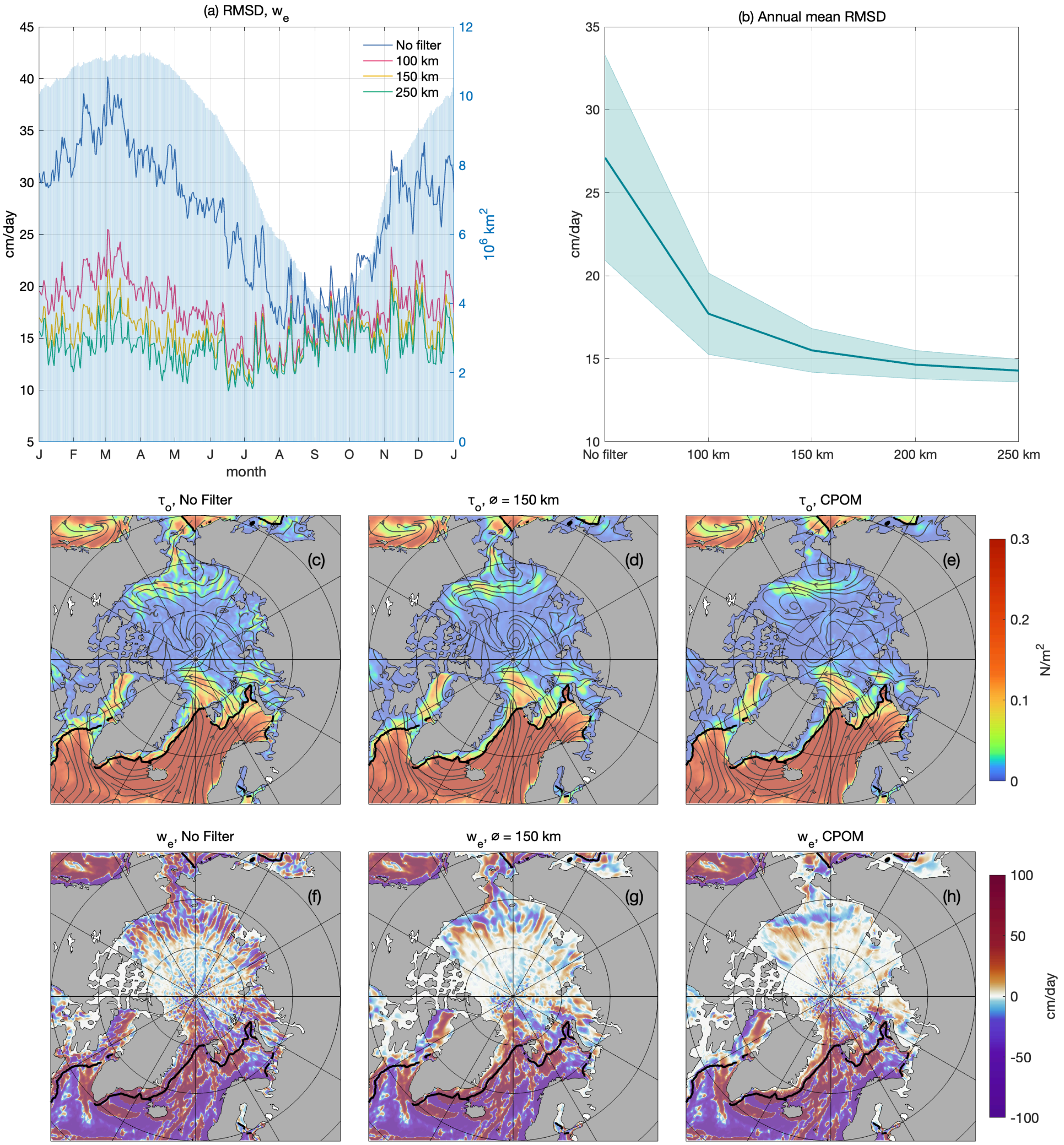

Figure 3: Area-averaged ocean-surface stress τ_o and vertical Ekman velocity w_e regarding Gaussian filter setting. (a) Annual cycle of root mean squared deviation (RMSD) of w_e over 2011. Blue shades show total ice-cover areas (right axis). (b) Annual mean RMSD of w_e with shading indicating one standard deviation over a year. (c) Snapshot of τ_o with unfiltered CLS (3/15/2011). (d) Same as c but with 150 km Gaussian filter. (e) Same as c but with CPOM. (f-h) Same as (c-e) but for w_e. Streamlines in (c-e) show the direction of τ_o. Black contours in (c-h) mark the 15% ice concentration on 3/15/2011.

https://doi.org/10.5194/essd-2025-14
Preprint. Discussion started: 6 February 2025

3 Results and Regional Statistics

3.1 Arctic Ocean

In this section, we provide a concise overview of the surface stress and the corresponding Ekman velocity fields. Figure 4a shows the time-averaged ocean-surface stress (τ_o) field across the Arctic for 2011–2018. The highest τ_o appears in the ice-free Nordic Seas, where strong wind-ocean interactions drive surface stress exceeding 0.3 N/m². In contrast, sea ice reduces momentum transfer and lower the τ_o in ice-covered regions. In the Seasonal Ice Zone (SIZ), marked by the March and September sea ice boundaries, τ_o typically remains below 0.05 N/m². Within the Perennial Ice Zone (PIZ), bounded by the September sea ice boundary, it drops further to below 0.02 N/m².

The seasonal cycle of τ_o is the dominant temporal variability across the Arctic (Stroeve and Notz, 2018). The standard deviation (STD) shows a spatial distribution similar to the time-averaged τ_o (Figure 4b), with high variability (>0.1 N/m²) in ice-free regions like the Nordic Seas. Variability is significantly suppressed in the SIZ and PIZ, with values below 0.02 N/m² and 0.01 N/m², respectively. The R^2 (the proportion of variance explained by the seasonal cycle) shows that in open-ocean regions, 40–60% of variance is explained by seasonal variability (Figure 4c). In ice-covered areas, this ratio drops to less than 30%.

The time-mean Ekman pumping rate (w_e), alongside its STD and R^2 patterns are given in Figure 4d-f. Strong upwelling (>50 cm/day) is observed in the Nordic Seas, while strong downwelling (<-10 cm/day) occurs in the Beaufort and Chukchi Seas. The spatial pattern of STD w_e is similar to that of τ_o (Figure 4e). Seasonal variability ranges from 10–20 cm/day in ice-free regions, 4–6 cm/day in SIZ, and falls below 4 cm/day in the PIZ. Seasonal variability accounts for up to 60% of w_e variance south of the Denmark Strait, but in other regions, including both ice-covered and ice-free zones, it typically explains 10–30%.

https://doi.org/10.5194/essd-2025-14
Preprint. Discussion started: 6 February 2025

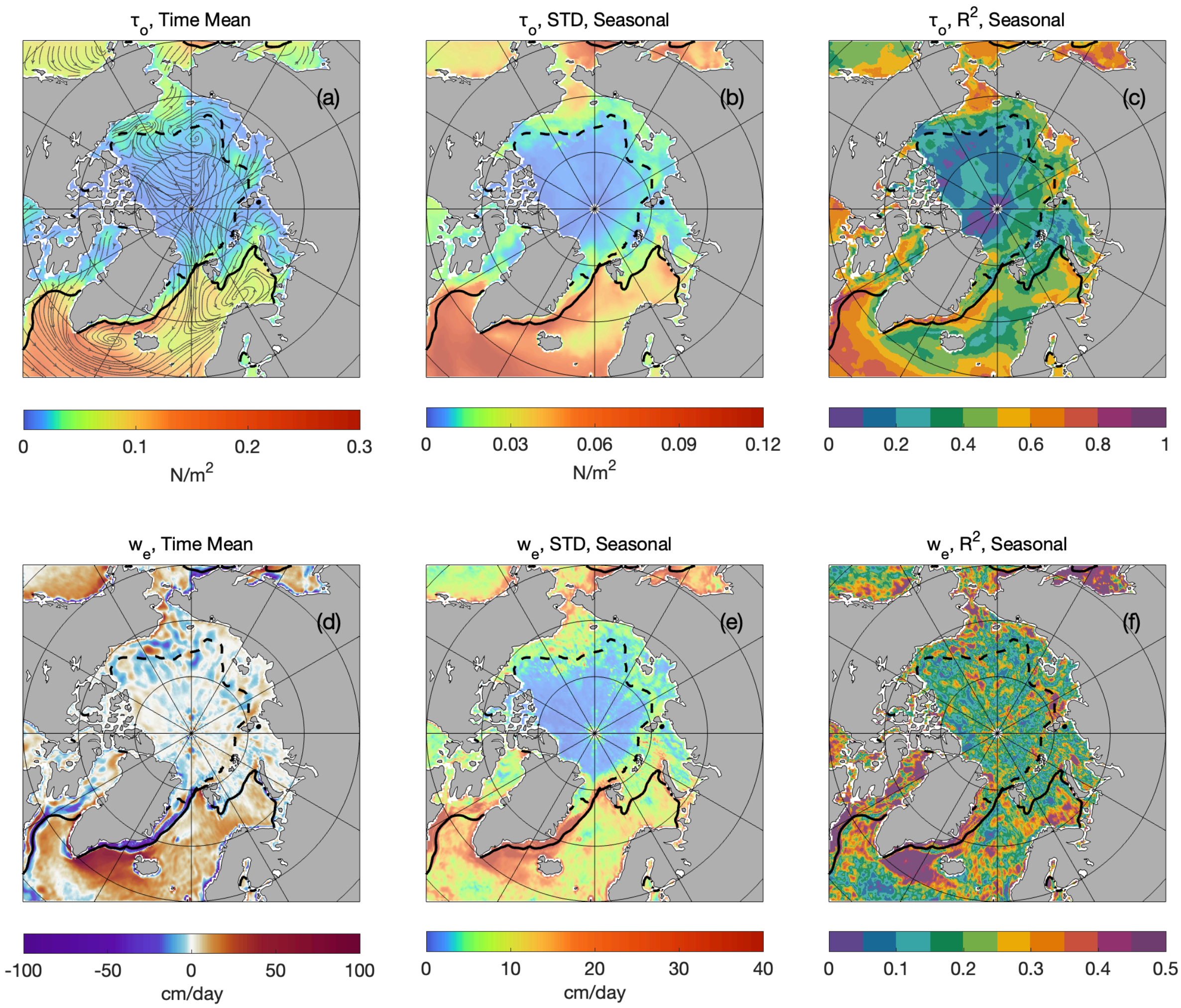

Figure 4: Mean and variability of ocean-surface stress τ_o and Ekman pumping rate w_e (positive indicates upwelling, negative indicates downwelling) in the Arctic region over 2011-2018. (a) Mean τ_o, with streamlines indicating the direction of stress. (b) Standard deviation of τ_o seasonal variability. (c) R^2, representing τ_o variance explained by seasonal variability. (d-f) Same as (a-c) but for w_e. Streamlines in (a) show the direction of τ_o. The solid and dashed black lines represent the March and September sea ice boundaries, respectively, defined by 15% sea ice concentration averaged over 2011-2018.

The seasonal cycle of area-averaged wind-ocean surface stress (τ_{aw}) is marked by strong values in winter, peaking around 0.4 N/m², and much weaker values in summer, dropping below 0.05 N/m² (Figure 5a). This variation corresponds to the seasonal retreat of sea ice and the associated expansion of open ocean during summer months.

In ice-covered regions, the seasonal cycle of ice-ocean surface stress (τ_{iw}) is similar to that of τ_{aw}, though with significantly lower magnitudes (Figure 5c). The seasonal peak of τ_{iw} is slightly higher in 2018 than 2013, increasing from 0.010 N/m² to nearly 0.018 N/m².

https://doi.org/10.5194/essd-2025-14
Preprint. Discussion started: 6 February 2025

In ice-free regions, the average pumping rate $w_{e,aw}$ peaks during winter upwelling, reaching around 30 cm/day, and transitions to weak downwelling during the summer (Figure 5e). Annual variation in winter maximum upwelling rate is evident, with a notable decline to 10 cm/day by late 2018 (Figure 5f). In contrast, in ice-covered regions, $w_{e,iw}$ is predominantly negative (Figure 5g), although occasional summer upwelling events occur on daily scales. Notably, the winter downwelling rate has decreased from approximately -8 cm/day in 2013–2014 to about -4 cm/day by 2017.

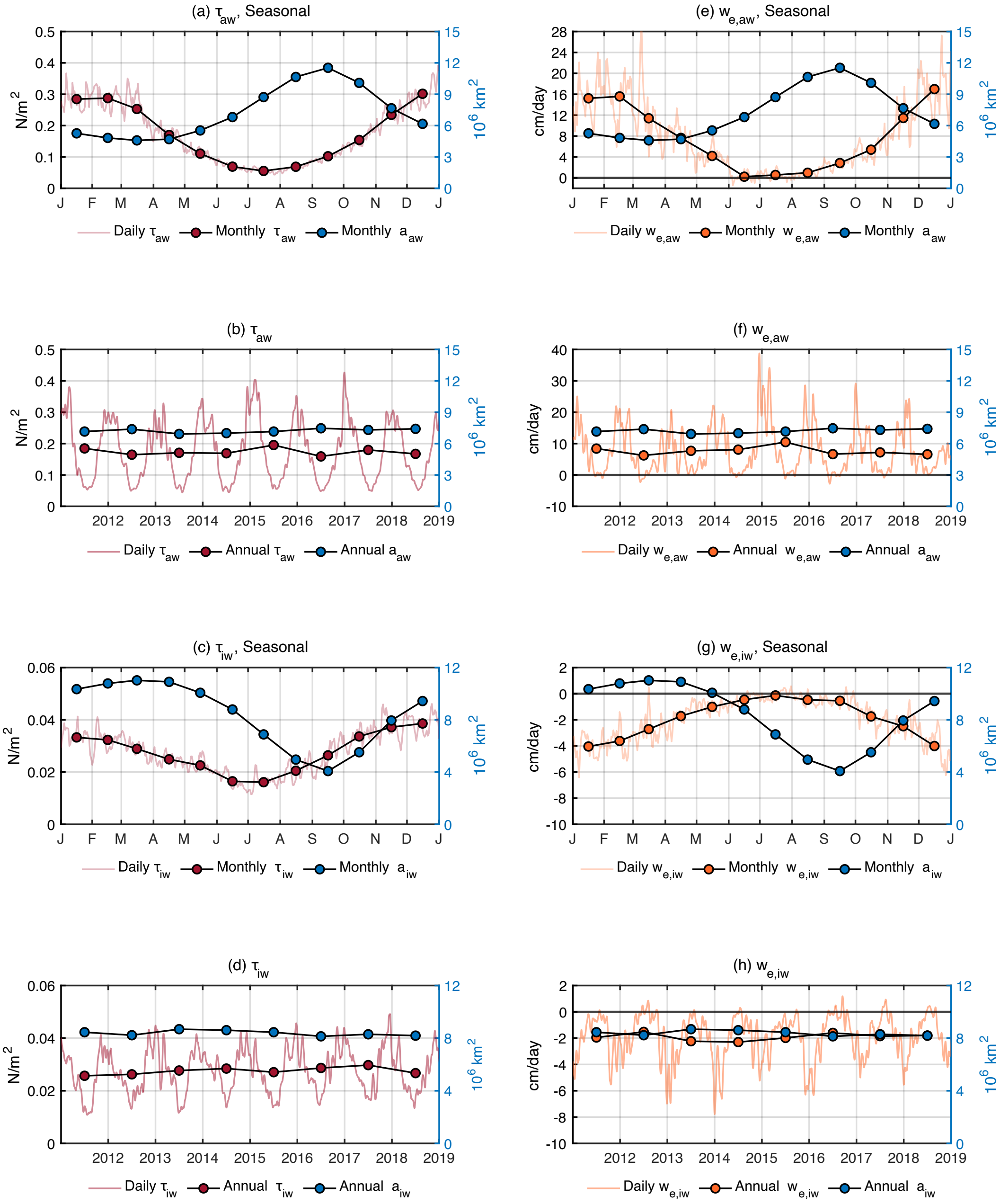

https://doi.org/10.5194/essd-2025-14
Preprint. Discussion started: 6 February 2025

Figure 5: Mean seasonal cycle and annual time series of area-averaged surface stress τ_o (red) and Ekman pumping rate w_e (orange, positive indicates upwelling, negative indicates downwelling) for the Arctic region. Total areas a of the corresponding areal coverage are also plotted in blue. Variables are subscripted aw when averaged/summed over ice-free open ocean, and are subscripted iw when averaged/summed over ice-covered open ocean. Annual and monthly means are shown as dots in all panels. (a) Seasonal cycle of τ_{aw} over the ice-free open ocean. (b) Timeseries of τ_{aw} from 2011-2018. (c) Seasonal cycle of τ_{iw} over the ice-covered ocean. (d) Timeseries of τ_{iw} from 2011-2018. (e-h) same as (a-d) but for w_e.

3.2 Southern Ocean

The spatial distribution of the time-mean τ_o in the Antarctic region is shown in Figure 6a. τ_o exhibits a prominent circumpolar pattern. In ice-free regions, τ_o typically ranges from 0.2 to 0.3 N/m². In the SIZ, τ_o decreases significantly, falling to 0.04–0.06 N/m², with strong regional variability.

The STD of τ_o seasonal variability is evidently strong near the September sea ice boundary, exceeding 0.1 N/m², particularly in the Indian Ocean sector and the southeast Pacific (Figure 6b). Moving northward into subpolar open-ocean, the STD gradually declines to approximately 0.04 N/m². Within the SIZ, seasonal variability diminishes further, typically ranging from 0.02 to 0.04 N/m². In the PIZ, it drops below 0.02 N/m². The R^2 shows that in regions such as the Indian Ocean and southeast Pacific, seasonality explains over 50% of the total variance, while in other areas, this proportion ranges from 20% to 40% (Figure 6c).

The spatial structure of the time-mean w_e reveals widespread upwelling south of 50°S (Figure 6d), extending nearly all the way to the coast of Antarctica. In contrast to the Arctic, where strong ice-ocean coupling leads to clear transitions between upwelling and downwelling across ice boundaries, the Southern Ocean does not exhibit this distinct pattern. Downwelling is generally found around 55°S and farther north, or more narrowly along the Antarctic coastline.

The STD pattern of seasonal variability in w_e is relatively consistent across the Southern Ocean (Figure 6e), regardless of sea-ice coverage, with an average value of approximately 10 cm/day. Higher variability, reaching up to 20 cm/day, occurs only near the September ice boundary and is very localized. The R^2 pattern is also relatively homogeneous, with most areas showing seasonal variability accounting for about 30% of the variance. Along the east coast of Antarctica, the seasonal cycle explains more than 50% of the variance.

https://doi.org/10.5194/essd-2025-14
Preprint. Discussion started: 6 February 2025

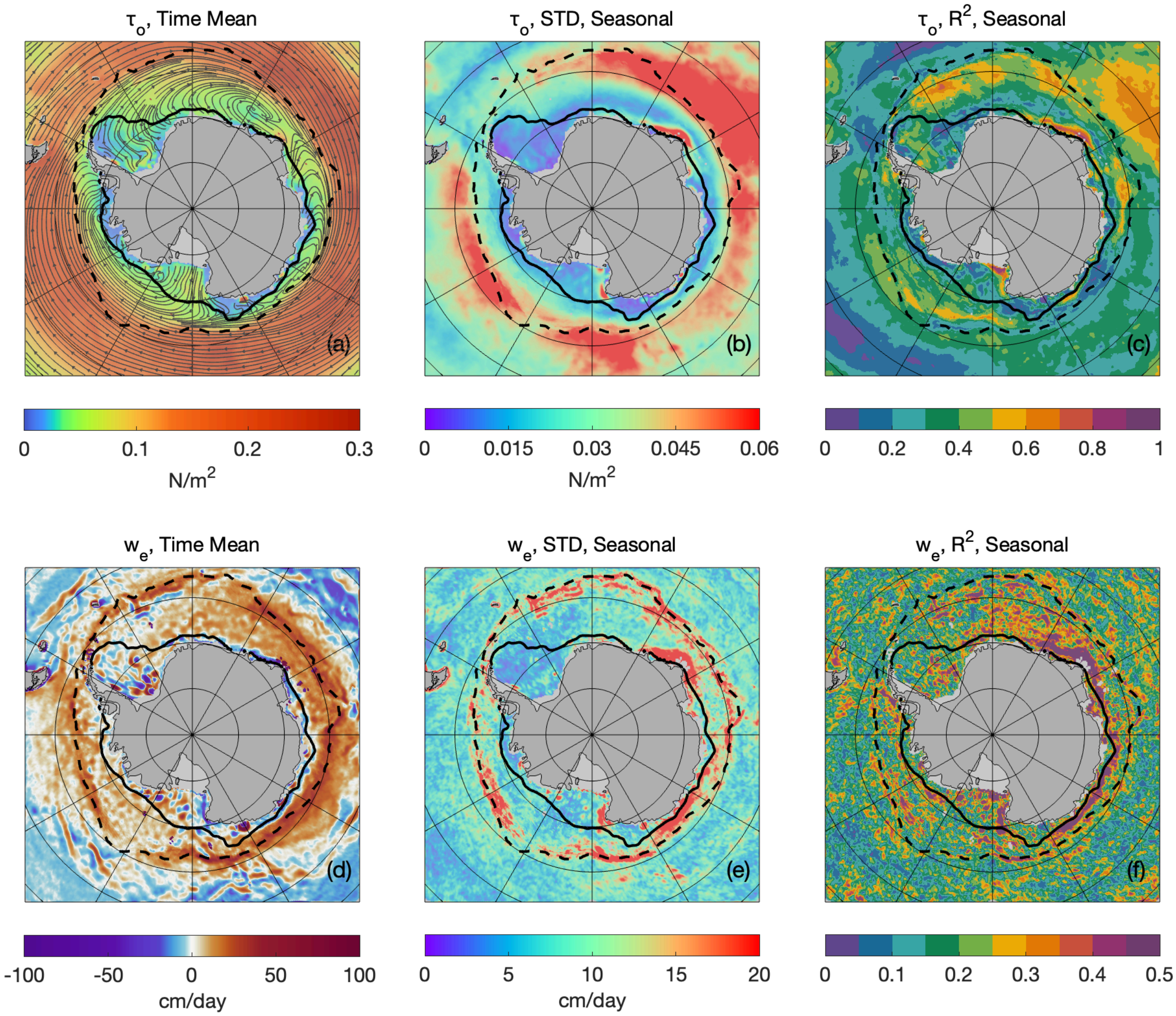

Figure 6: Mean and variability of ocean-surface stress τ_o and Ekman pumping rate w_e (positive indicates upwelling, negative indicates downwelling) in the Antarctic region over 2013-2018. (a) Mean τ_o, with streamlines indicating the direction of stress. (b) Standard deviation of τ_o seasonal variability. (c) R^2, representing τ_o variance explained by seasonal variability. (d-f) Same as (a-c) but for w_e. Streamlines in (a) show the direction of τ_o. The solid and dashed black lines represent the March and September sea ice boundaries, respectively, defined by 15% sea ice concentration averaged over 2013-2018.

The seasonal cycle and time series of area-averaged air-water stress τ_{aw} in the Antarctic are shown in Figures 7a and 7b. In ice-free regions of the Antarctic, the average τ_{aw} peaks in August at 0.36 N/m² and reaches its minimum in January at 0.13 N/m². Annual variability is relatively small, ranging between 0.022 and 0.026 N/m², with a notable positive anomaly in 2015, when the annual mean briefly increased to 0.028 N/m².

In ice-covered regions, ice-water stress τ_{iw} shows a delayed seasonal cycle compared to τ_{aw} and peaks in September (Figure 7c). It is approximately one-fifth to one-half of τ_{aw}, ranging between 0.02 N/m² and 0.08 N/m². The seasonal pattern is

https://doi.org/10.5194/essd-2025-14
Preprint. Discussion started: 6 February 2025

asymmetrical and aligns with the seasonal cycle of sea ice coverage (Eayrs et al., 2019). Similar to the Arctic, the area-averaged summer minima of τ_{iw} is slightly higher in 2018 compared to 2013, increasing from 0.010 N/m² in to 0.022 N/m². The seasonal cycle of open-ocean Ekman pumping rate $w_{e,aw}$ is relatively weak (Figure 7e), with higher values in winter (12 cm/day) and lower values in summer (5 cm/day). The absence of a distinct seasonal signal is likely due to the weaker seasonal cycle observed in 2017 and 2018 (Figure 7f). The annual mean varies narrowly between 7 and 9 cm/day. In ice-covered regions, $w_{e,iw}$ is mostly positive throughout the year, with a brief downwelling period between January and April. A shift toward stronger downwelling occurs in February, with mean values decreasing from -2 cm/day in 2013 to nearly -10 cm/day by 2017. A notable anomaly occurred in 2015 when the annual mean rose sharply from 2 cm/day to 4 cm/day.

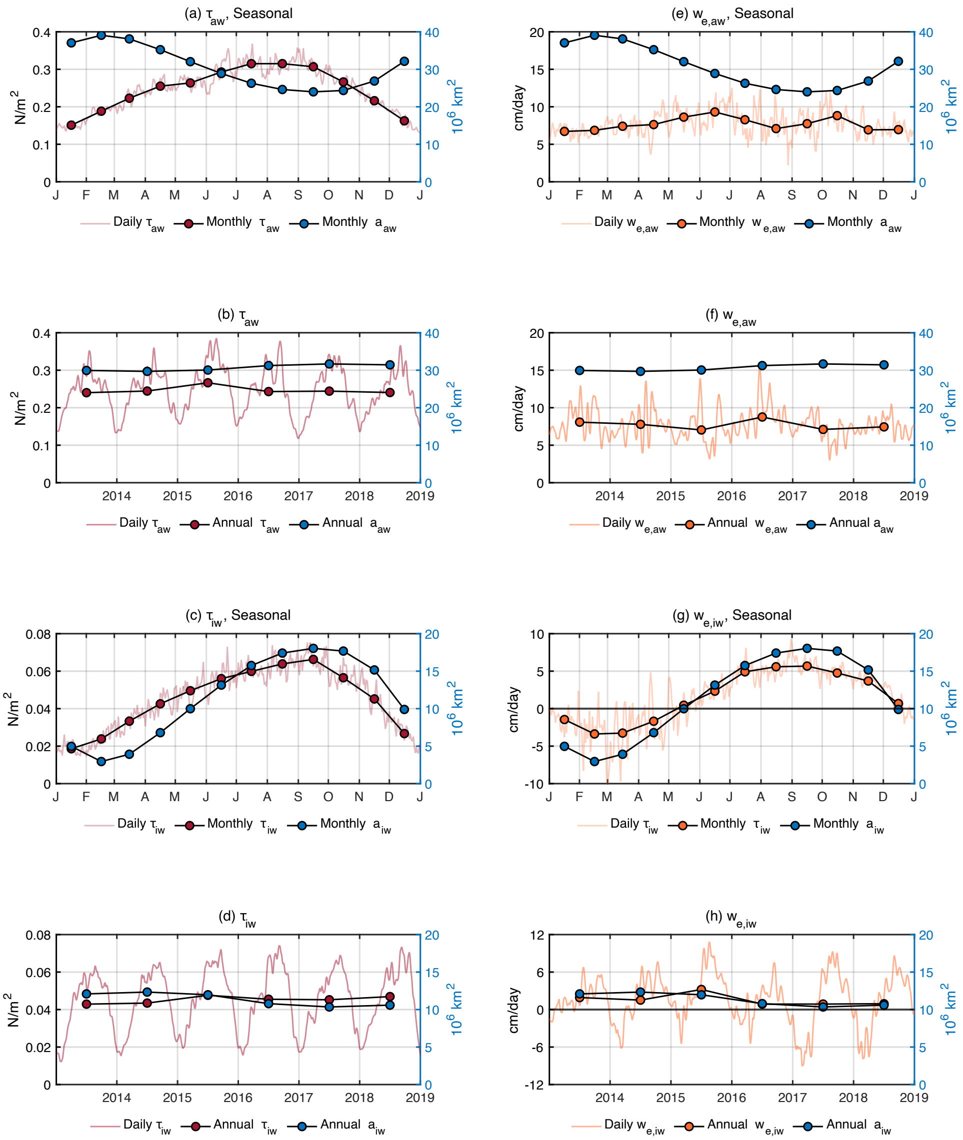

https://doi.org/10.5194/essd-2025-14
Preprint. Discussion started: 6 February 2025

Figure 7: Timeseries and seasonal cycle of area-averaged surface stress τ_o (red) and Ekman pumping rate w_e (orange, positive indicates upwelling, negative indicates downwelling) for the Antarctic region. Total areas a of the corresponding areal coverage are also plotted in blue. Variables are subscripted aw when averaged/summed over ice-free open ocean, and are subscripted iw when averaged/summed over ice-covered open ocean. Annual and monthly means are shown as dots in all panels. (a) Seasonal cycle of τ_{aw} over the ice-free open ocean. (b) Timeseries of τ_{aw} from 2013-2018. (c) Seasonal cycle of τ_{iw} over the ice-covered ocean. (d) Timeseries of τ_{iw} from 2013-2018. (e-h) same as (a-d) but for w_e.

4 Uncertainty and Data Quality Assessment

4.1 Sensitivity Analysis of Ice-Water Drag Coefficient and uncertainty estimate

The ice-water drag coefficient, $C_{D,iw}$ is often assumed to be constant across time and space due to the scarcity of direct observations that capture its spatiotemporal variability. However, $C_{D,iw}$ can vary significantly depending on environmental conditions such as wind and wave dynamics, ice roughness, sea ice concentration, and surface morphology (Lüpkes et al., 2012; Lüpkes and Birnbaum, 2005; Cole & Stadler, 2019). Reported values for $C_{D,iw}$ range from 0.7 to over 10.0×10^{-3} (Overland, 1985; Guest and Davidson, 1987, 1991; McPhee, 2008; Cole et al., 2014), with some extreme cases reaching magnitudes on the order of 10.0×10^{-1} (Kawaguchi et al., 2024).

Commonly, a representative value of 5.5×10^{-3} has been widely adopted as a pragmatic approximation by the scientific community (Guest and Davidson, 1987; Anderson, 1987). However, this approximation may overlook important spatial and temporal variations in $C_{D,iw}$, highlighting the need for ongoing efforts to improve observations and refine its parameterization.

To evaluate the sensitivity of estimated τ_o to the variations in $C_{D,iw}$, two sets of experiments are conducted for 2011: one with fixed $C_{D,iw}$ values ranging from 1.0×10^{-3} to 10.0×10^{-3}, and another using a randomized weighting map, dynamically varying $C_{D,iw}$ between between order of 10^{-3} and 10^{-2} on a daily basis at each grid cell.

The amplitude of τ_o scales proportionally with $C_{D,iw}$, as implied from Eq. 2 (Figure 8a). For fixed coefficients, the summer mean τ_o increases from 0.003 N/m² at $C_{D,iw} = 1.0 \times 10^{-3}$, to 0.015 N/m² at $C_{D,iw} = 10.0 \times 10^{-3}$, while winter means rise from 0.012 N/m² to 0.053 N/m². Results from the random-weighted $C_{D,iw}$ experiment closely follows the fixed cases of $C_{D,iw} = 5.0$-6.0×10^{-3}. Similarly, the annual mean τ_o and its standard deviation increase proportionally with $C_{D,iw}$ (Figure 8b), quadrupling the annual mean and raising the standard deviation from 0.003 N/m² to 0.017 N/m² as $C_{D,iw}$ increases.

Figures 8c–h show the spatial distribution of τ_o and w_e in response to varying $C_{D,iw}$. Under low $C_{D,iw}$ circumstances, momentum transfer between ice and ocean is reduced, leaving small scale variability indistinct particularly in the central Arctic. As $C_{D,iw}$ increases, regions with high surface stress intensify, particularly in areas like Baffin Bay, the Chukchi Sea, and north of Fram Strait.

At $C_{D,iw} = 1.0 \times 10^{-3}$, the Ekman pumping rate in regions like the Fram Strait barely reach ±8 cm/day, whereas at $C_{D,iw} = 10.0 \times 10^{-3}$, it exceeds ±30 cm/day, with strong contrasting upwelling and downwelling patterns. additionally, while the random-

https://doi.org/10.5194/essd-2025-14
Preprint. Discussion started: 6 February 2025

weighted $C_{D,iw}$ experiment introduces spatial noise, the broader spatial structures of both τ_o and w_e remain consistent with fixed-coefficient runs.

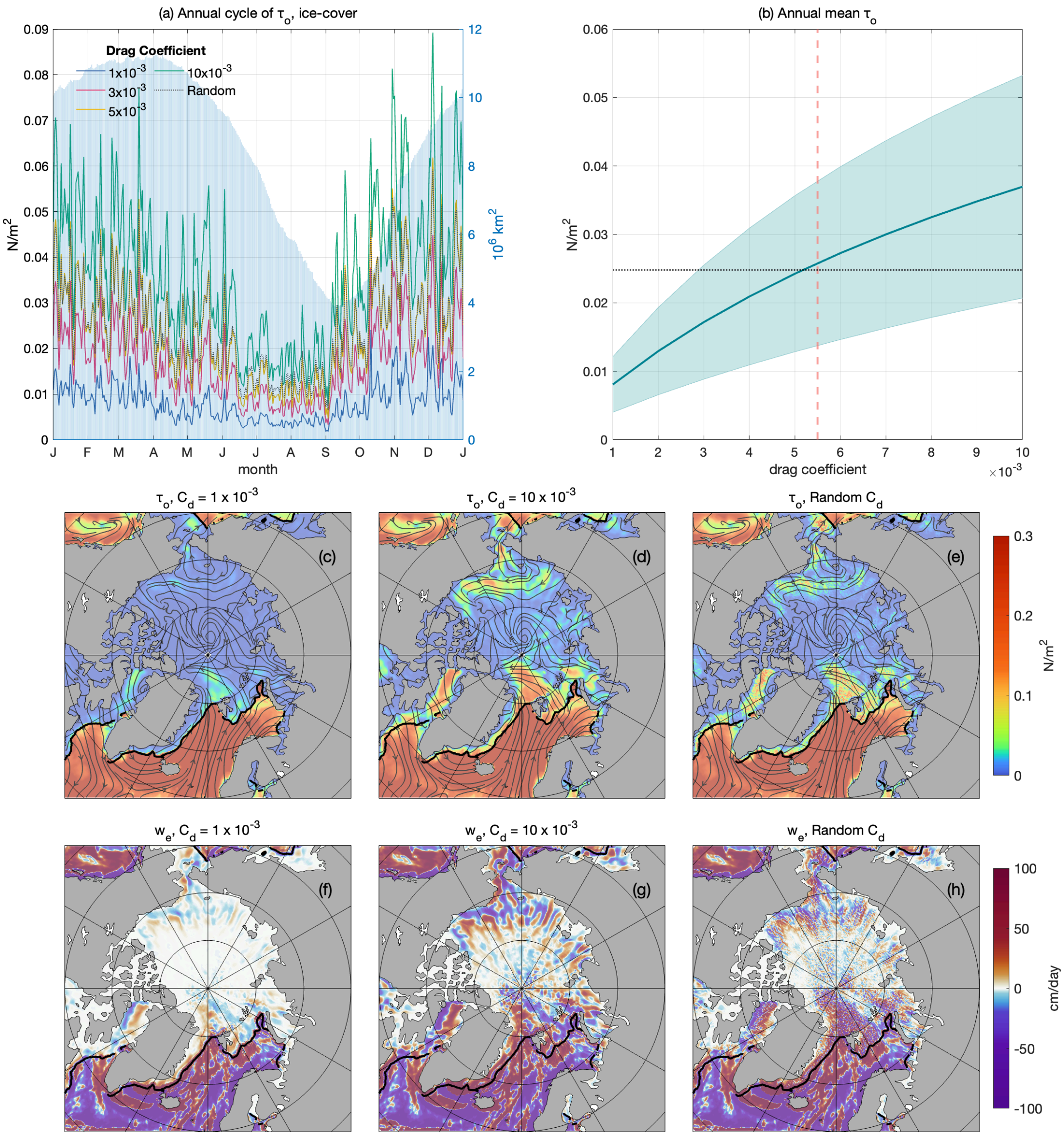

Figure 8: Area-averaged ocean-surface stress τ_o and Ekman pumping rate w_e regarding different $C_{D,iw}$. (a) annual cycle of τ_o of 2011, area-averaged over the sea ice-cover region. Blue areas show total ice-cover areas (right axis); (b) annual mean of τ_o with shading indicating one standard deviation over a year. Red dashed line marks $C_{D,iw}$ = 5.5 × 10^{-3}, black dotted line shows the annual mean of random $C_{D,iw}$ experiment. (c) Snapshot of τ_o with $C_{D,iw}$ = 1.0 × 10^{-3} (3/15/2011). (d) Same as c but with $C_{D,iw}$ = 10.0 × 10^{-3} . (e) Same as c but with random $C_{D,iw}$. (f-h) Same as (c-e) but for w_e. Streamlines in (c-e) show the direction of τ_o. Black contours in (c-h) mark the 15% ice concentration on 3/15/2011.

https://doi.org/10.5194/essd-2025-14
Preprint. Discussion started: 6 February 2025

The final estimated uncertainty ε_{iw}, in the ice-water stress τ_{iw} is quantified daily through the integration of standard errors from sensitivity analyses of $C_{D,iw}$ and spatial Gaussian filter tests. Both filter tests and $C_{D,iw}$ tests are extended to the full eight-year/six-year period. Using the root-sum-square method, the combined uncertainty is expressed as:

$$\varepsilon_{iw} = \sqrt{(\varepsilon_{iw,F})^2 + (\varepsilon_{iw,C})^2} = \sqrt{(\frac{\sigma_F}{\sqrt{N_1}})^2 + (\frac{\sigma_C}{\sqrt{N_2}})^2} \quad (7)$$

where σ_F is the standard deviation of τ_{iw} from different Gaussian filter settings, and σ_C represents the standard deviation of τ_{iw} from sensitivity analysis on varying $C_{D,iw}$. The terms N_1 and N_2 denote the number of runs performed in each sensitivity analysis. This estimate assumes independence between $C_{D,iw}$ and geostrophic fields (which were spatially filtered), with perturbations of comparable amplitude between the two sets of sensitivity analysis.

Figure 9 shows the spatial distributions of relative uncertainty (ε_{iw} to τ_{iw}) for the Arctic (March 15, 2013) and the Southern Ocean (September 15, 2013) during winter season. Overall, spatial filtering produces scattered patterns (Figures 9a–9d), while varying ice-water drag coefficient yield smoother distributions (Figures 9e–9h). Median uncertainties are comparable between the two sets of experiments, ranging from 14–18% in the Arctic to 22–25% in the Antarctic. The greater uncertainties in the Antarctic reflect higher local stress variability and increased sensitivity to parameter changes, which also manifests as the higher uncertainties observed in winter compared to summer (Figures 3 and 8).

In the Arctic, combined uncertainties for zonal surface stress (τ_x) typically range from 10–20%, while locally it could exceed 100% along dynamic regions such as the Fram Strait and Beaufort Sea. Meridional stress (τ_y) exhibits similar spatial distributions, but with higher uncertainties near the Mendeleev Ridge. Median uncertainty levels for both zonal and meridional components are below 20%.

Conversely, Antarctic uncertainties are substantially higher, with median values around 40%. The highest uncertainties (>60%) are concentrated near the sea ice boundary, particularly in the eastern Weddell and Ross Seas. Regional hotspots include the Antarctic Peninsula and western Ross Sea for τ_x, and Enderby Land and the Amundsen Sea for τ_y.

Noting these uncertainties come from gridding and theoretical assumption, and are not accounted for the uncertainty from the input datasets. For instance, ice motion typically carries significant uncertainties in both speed and angle, varying substantially across different datasets (Sumata et al., 2014; Wang et al., 2022).

https://doi.org/10.5194/essd-2025-14
Preprint. Discussion started: 6 February 2025

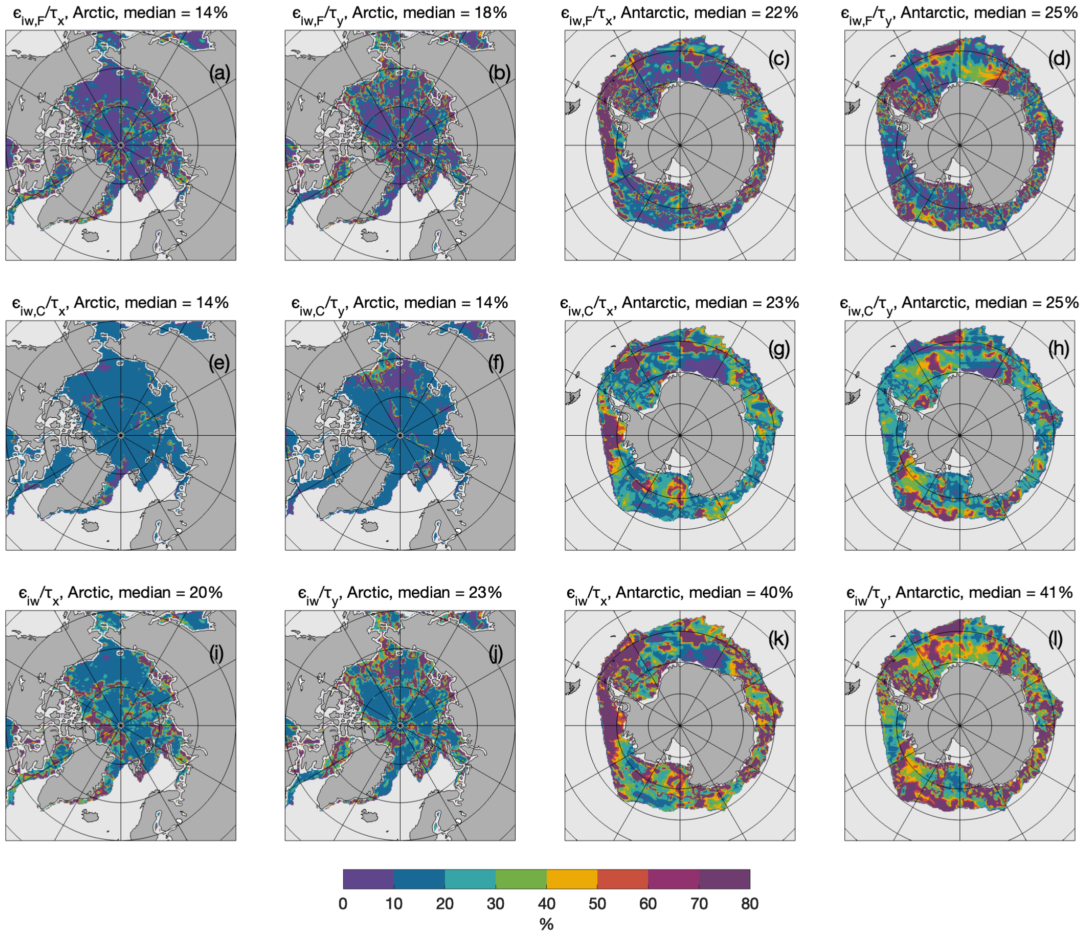

Figure 9: Estimated uncertainty fields for zonal and meridional ice-water surface stress, expressed as a ratio to the estimated ice-water surface stress in the Arctic (3/15/2013) and Southern Ocean (9/15/2013). (a) standard error introduced by Gaussian filter in the Arctic, zonal direction; (b) error from filter in the Arctic, meridional direction; (c-d) same as (a-b) but for the Antarctic; (e-h) same as (a-d) but for standard error in ice-water drag coefficient $C_{D,iw}$; (i-l) same as (a-d) but for the combined uncertainty.

4.2 Validation with ITP Observations

Since surface stress is not usually directly measured, assessing the performance of our analysis is challenging. To address this, we revisit the assumption that surface velocity comprises both Ekman and geostrophic components, as described in Eq. (2). The geostrophic velocity (U_g) is derived from the dataset provided by Prandi et al. (2021), while the Ekman velocity component (U_e) can be easily calculated from the ocean-surface stress using Eq. (4).

This assumption provides a first-order approximation of surface velocity, and neglects other processes, such as ageostrophic motions, vertical shear, and submesoscale dynamics, which may introduce additional uncertainties. Here we compare the

https://doi.org/10.5194/essd-2025-14
Preprint. Discussion started: 6 February 2025

satellite retrieved surface velocity, i.e., sum of U_g and U_e, against velocity profiles obtained from Ice-Tethered Profilers (ITP, Krishfield et al., 2008; Toole et al., 2011; http://www.whoi.edu/itp), which includes velocity sensors (ITP-V) as described by Williams et al. (2010). Noting this comparison does not necessarily validate the accuracy of our stress analysis but rather evaluates whether the simplified assumptions underlying the methodology adequately capture the complex dynamics of the Arctic Ocean.

Table 2: Details of the ITP-V records

Unit ID	Start		Last		# of Days	# of Profiles
	Position	Date	Position	Date		
ITP-70	76.81°N 138.89°W	8/26/2013	77.11°N 156.51°W	7/15/2014	324	3713
ITP-77	73.37°N 134.99°W	3/11/2014	75.89°N 158.50°W	10/2/2014	206 (153*)	2367 (1800*)
ITP-78	74.36°N 135.14°W	3/12/2014	74.08°N 145.43°W	8/6/2014	148 (130*)	1694 (1500*)
ITP-79	75.38°N 136.50°W	3/22/2014	75.02°N 148.37°W	9/30/2014	193 (143*)	1694 (1636*)
ITP-80	77.36°N 146.15°W	8/14/2014	75.68°N 151.79°W	5/24/2015	284	3260

* Data towards the end of the series exhibits quality issues that necessitate truncation.

https://doi.org/10.5194/essd-2025-14
Preprint. Discussion started: 6 February 2025

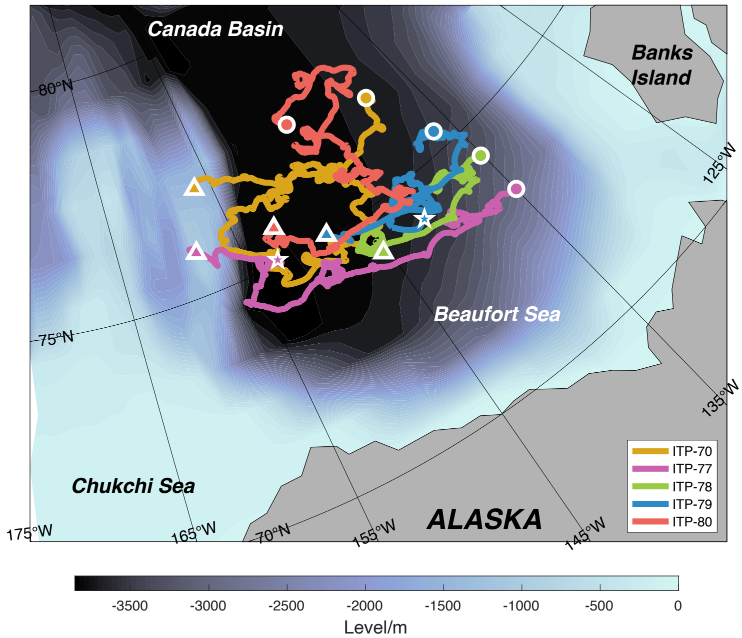

Figure 10: ITP-V drift tracks in the Arctic Ocean (colored curves). The deployment locations are marked by circles, latest locations by triangles, and the cutoff locations for ITP-77 and ITP-79 by stars.

We use velocity data collected from five ITP-V missions deployed on multiyear sea ice in the Canada Basin between 2011 and 2019 (Figure 10; Table 2). Observations from ITP-77, ITP-78, and ITP-79 are truncated to exclude periods with significant data gaps and drifts near the end of their deployments.

The five ITP-Vs are categorized into two groups based on deployment timing and drift trajectories. ITP-70 and ITP-80 were deployed during summer, operated for ~300 days, and primarily drifted between 75–80°N. In contrast, ITP-77, ITP-78, and ITP-79, deployed in March 2014, operated for less than 200 days and followed more constrained east-to-west trajectories between 73–75°N.

The satellite-derived velocity, U_g+U_e, is temporally interpolated to pair with the ITP sampling frequency (2–6 hours) and then extracted at the nearest grid point along each track (Figure 11). For ITP-70 and ITP-80 pairs, satellite-derived velocity shows moderate agreement, particularly in high-frequency signals. For ITP-77, ITP-78, and ITP-79 pairs, the agreement is weaker, especially in the zonal components. In the meridional components, ITP-77 exhibits better agreement during the first 100 days. The reduced agreement for ITP-77, ITP-78, and ITP-79 pairs can be attributed to several factors. The coarse spatial resolution of the satellite data (25 km, daily) may limit its ability to capture small-scale velocity variations. Second, the March deployment period coincides with heightened kinetic energy in the Beaufort Gyre (Cassianides et al., 2023), leading to increased eddy activity in the Canada Basin (Son et al., 2022; Regan et al., 2020), which likely contributed to the large velocity variation captured by ITPs.

https://doi.org/10.5194/essd-2025-14
Preprint. Discussion started: 6 February 2025

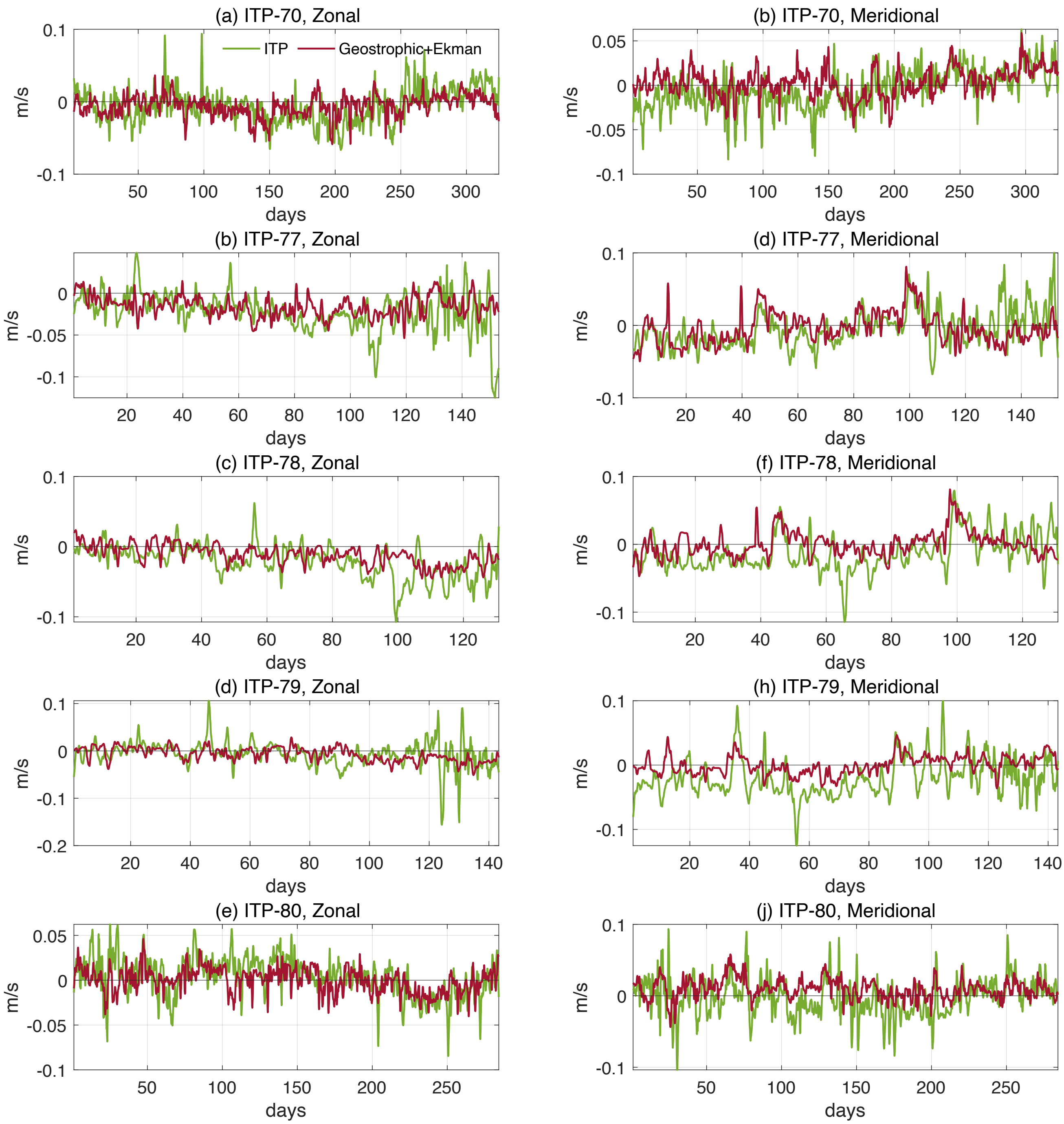

Figure 11: Timeseries of zonal and meridional surface velocity. (a) Zonal velocity along ITP-70 track. (b) Zonal velocity along ITP-77 track. (c) Zonal velocity along ITP-78 track. (d) Zonal velocity along ITP-79 track. (e) Zonal velocity along ITP-80 track. (f-j) same as (a-e) but for meridional velocity. Green curves represent velocity data retrieved from ITPs. Red curves are collocated obtained from the satellite-derived velocity fields, i.e., geostrophic plus Ekman velocity.

https://doi.org/10.5194/essd-2025-14
Preprint. Discussion started: 6 February 2025

Figures 12 and 13 present scatterplots comparing the paired observations of each ITP-V with satellite-derived velocity components. In general, ITP-70 and ITP-80 pairs (Figure 12) demonstrate better linear relationships compared to the other ITP-Vs (Figure 13). In all cases, satellite-derived velocity has a weak northward bias.

For ITP-70 pair, a notable pattern emerges after 200 days, with better consistency particularly in the meridional (and northward) direction. Similarly, ITP-80 pair shows better agreement in the zonal component after 200 days. These patterns align with the trajectory data in Figure 10, which show predominantly northward and westward movements for ITP-70 and ITP-80, respectively, during this period. In contrast, the other three ITP pairs exhibit weaker correlations with satellite-derived velocity (Figure 13). Satellite-derived velocity also underestimates the surface velocity observed by ITPs, particularly after 100 days.

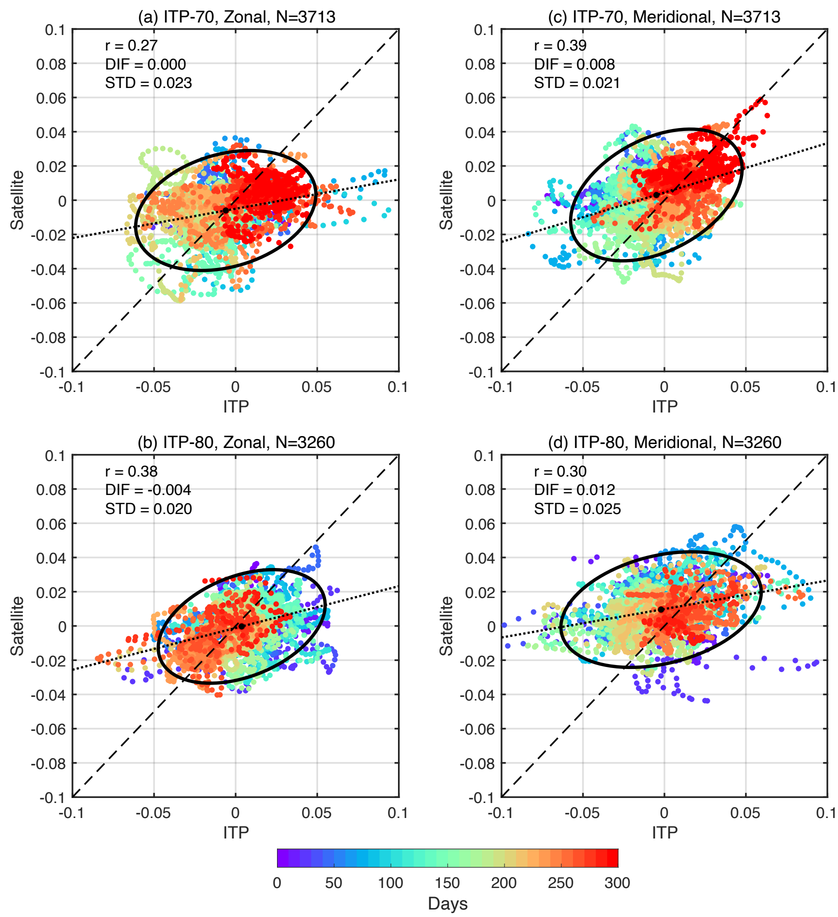

Figure 12: Scatterplots of collocated surface velocity pairs for ITPs with data spanning more than 200 days (unit: m/s). (a) Zonal velocity along ITP-70 track. (b) Zonal velocity along ITP-80 track. (c-d) Same as (a-b) but for meridional velocity. The total number of collocation pairs (N) is given. Correlation coefficients, mean differences (DIF), and standard deviations (STD) of the differences between satellite-derived velocity and ITP observations are also displayed. 95% confidence ellipse (black contour), linear fitting (black dotted line) are also given in each panel.

https://doi.org/10.5194/essd-2025-14
Preprint. Discussion started: 6 February 2025

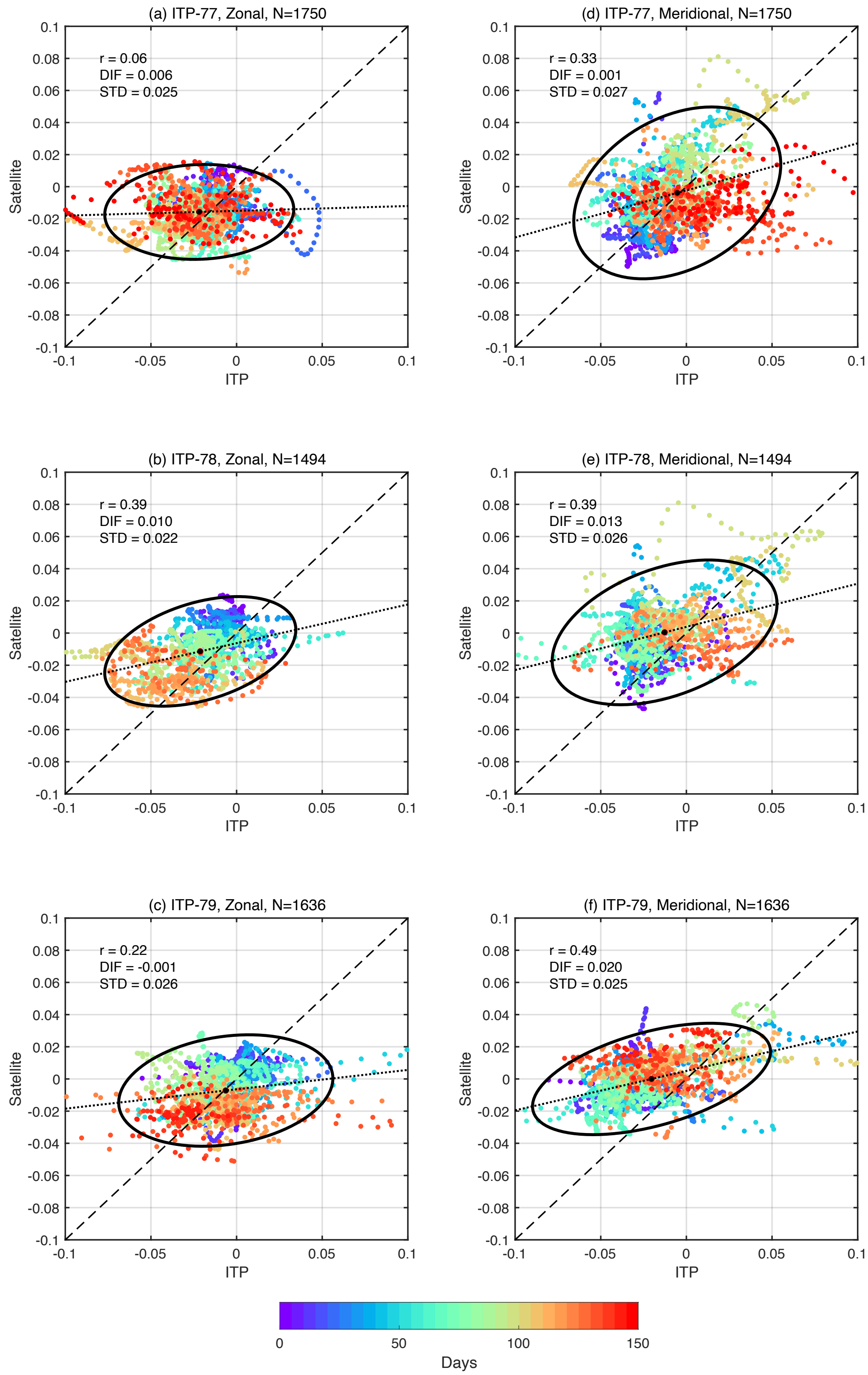

397

https://doi.org/10.5194/essd-2025-14
Preprint. Discussion started: 6 February 2025

Figure 13: Scatterplots of collocated surface velocity pairs for ITPs with data spanning less than 200 days (unit: m/s). (a) Zonal velocity along ITP-77 track. (b) Zonal velocity along ITP-78 track. (c) Zonal velocity along ITP-79 track. (d-f) Same as (a-c) but for meridional velocity. The total number of collocation pairs (N) is given. Correlation coefficients, mean differences (DIF), and standard deviations (STD) of the differences between satellite-derived velocity and ITP observations are displayed. 95% confidence ellipse (black contour), linear fitting (black dotted line) are also given in each panel.

Table 3 and Figure 14 summarize the velocity comparison between satellite-derived estimates and ITP-V observations. A consistent northward bias is evident in the satellite-derived velocity. The meridional velocity aligns closely with ITP measurements, but the zonal component (ITP-77 and ITP-78) exhibits a weak eastward bias. Satellite-derived velocity also have lower standard deviations than ITP-V measurements, indicating reduced variability.

Satellite-derived velocity explain a substantial portion of the variance in ITP-V measurements with averaging R^2 at 0.5, and reaching as high as 0.8 for the zonal component (ITP-78) and 0.7 for the meridional component (ITP-79). These results demonstrate the analysis's ability to capture significant variability, even though correlation coefficients between satellite and ITP velocity remain modest, mostly ranging from 0.3 to 0.4.

Table 3: Comparison of satellite-derived velocity to the ITP velocity along the ITP tracks. Numbers in the bracket are from the velocity fields without spatial filter. Correlations (*r*) with *p*<0.05 are in bold.

ITP-Vs		Mean (ITP)	Mean (Sat.)	STD (ITP)	STD (Sat.)	r	R^2
ITP-70	Zonal	-0.006	-0.006	0.023	0.014	**0.27**	0.58
	Meridional	-0.005	-0.003	0.021	0.016	**0.39**	0.36
ITP-77	Zonal	-0.022	-0.016	0.023	0.012	0.06	0.36
	Meridional	-0.005	-0.004	0.025	0.022	**0.33**	0.32
ITP-78	Zonal	-0.021	-0.011	0.023	0.014	**0.39**	0.80
	Meridional	-0.013	0.001	0.027	0.018	**0.39**	0.44
ITP-79	Zonal	-0.006	-0.007	0.026	0.014	**0.22**	0.39
	Meridional	-0.020	-0.001	0.028	0.014	**0.49**	0.73
ITP-80	Zonal	-0.004	-0.001	0.021	0.014	**0.38**	0.65
	Meridional	-0.002	0.010	0.025	0.014	**0.30**	0.20
Mean	Zonal	-0.010	-0.008	0.023	0.014	0.27	0.55
	Meridional	-0.009	0.002	0.025	0.017	0.38	0.41

https://doi.org/10.5194/essd-2025-14
Preprint. Discussion started: 6 February 2025

Open Access Earth System Science Data Discussions

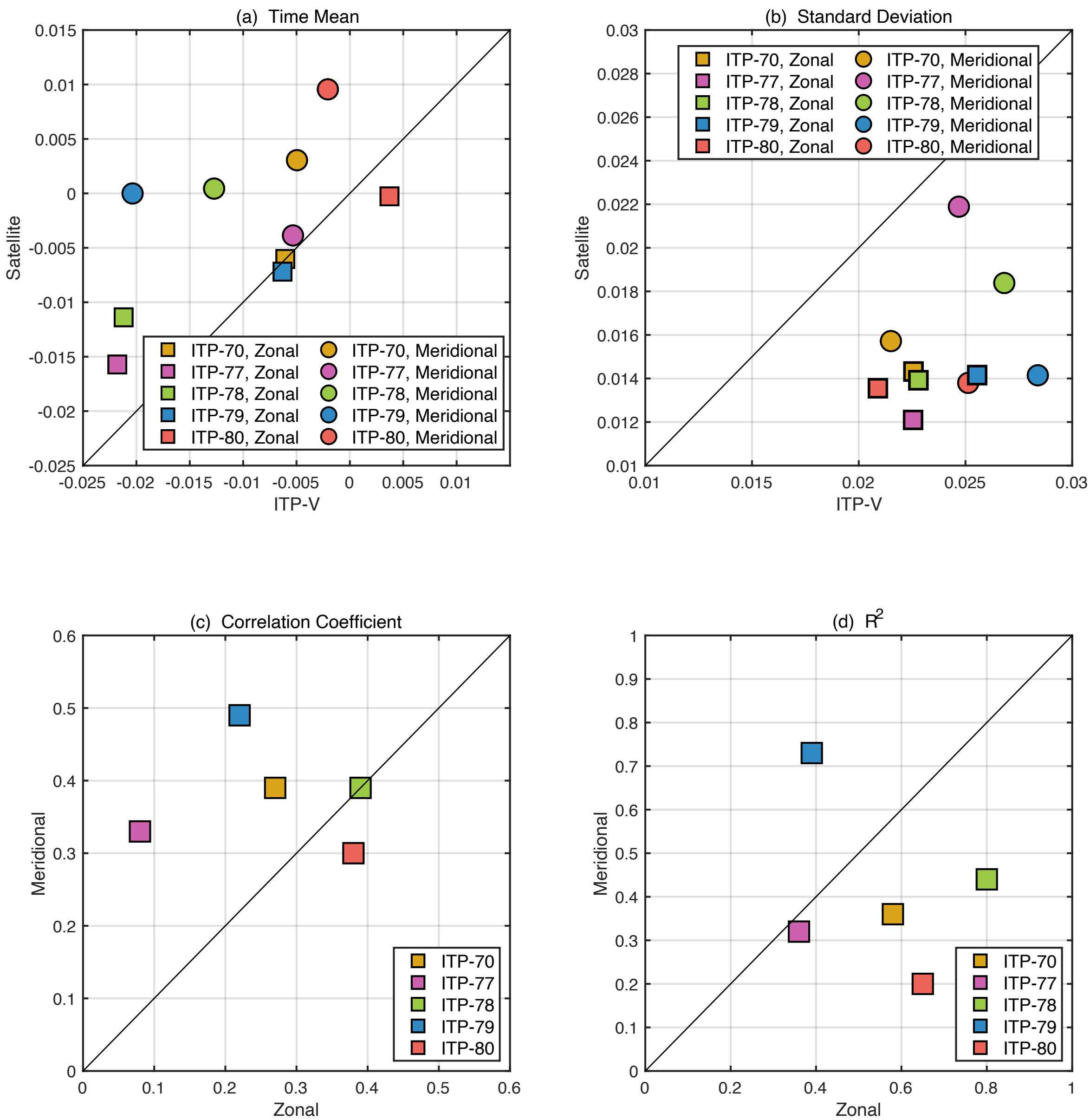

416

417 **Figure 14: Scatterplots of statistics of satellite-derived velocity and the ITP velocity. (a) Temporal mean and (b) standard deviation**
418 **of the paired velocity (unit: m/s). (c) Correlation between satellite-derived velocity and the ITP velocity. (d) Coefficient of**
419 **determination (R^2) of the variation in the ITPs explained by satellite-derived velocity.**
420
421

422 Additionally, satellite-derived velocity shows stronger correlations with ITP measurements when analyzed over longer
423 timescales, such as monthly averages or more. Applying a 30-day low-pass filter to both datasets improves the overall
424 agreement, with correlation coefficients exceeding 0.8 ($p<0.05$) for zonal geostrophic velocity from ITP-70, ITP-78, and ITP-
425 80 pairs, and over 0.7 ($p<0.05$) for the meridional component of ITP-79 pair (Figure 15). This could come from strong seasonal

https://doi.org/10.5194/essd-2025-14
Preprint. Discussion started: 6 February 2025

signals in ocean dynamics. The additional application of a 30-day low-pass filter reduces the influence of short-term, small-scale features, aligning satellite observations closely with smoothed patterns in ITP measurements.

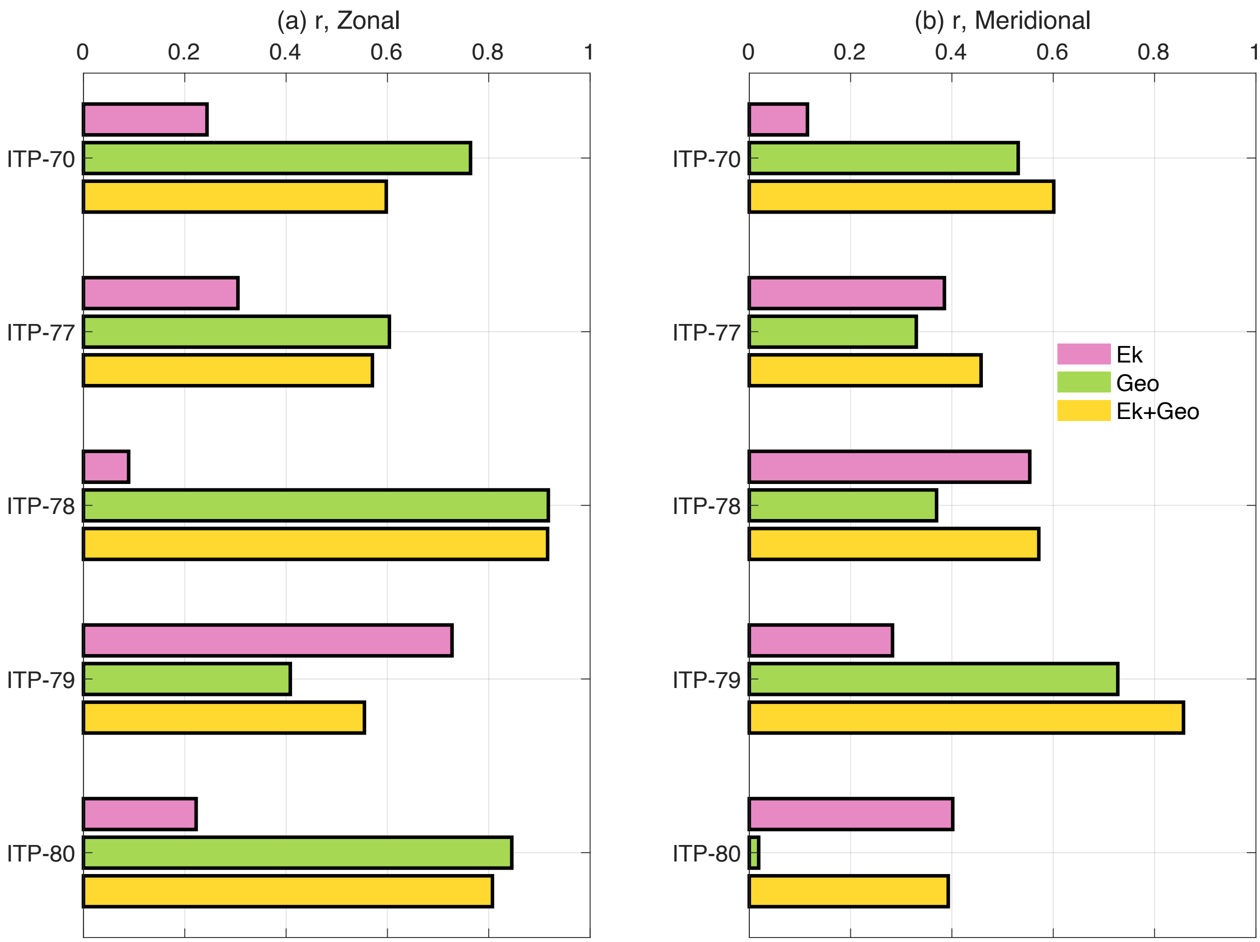

Figure 15. Bar chart of the correlation coefficient between the timeseries of ITP-V velocity and the satellite-derived velocity. A 30-day low pass filter is applied to all timeseries. The Ekman and the geostrophic components of the satellite-derived velocity are also compared.

5 Data Availability

Daily fields of ocean-surface stress vectors and derived vertical Ekman velocity for the polar oceans are provided for two periods: 2011–2018 for the Arctic (EPSG number 3408) and 2013–2018 for the Antarctic (EPSG number 3409) and are available at https://doi.org/10.5281/zenodo.14750492 (Liu & Yu, 2024). The datasets include three auxiliary fields: (i) land mask, (ii) grid longitudes and latitudes, and (iii) uncertainty estimates for ocean-surface stress.

https://doi.org/10.5194/essd-2025-14
Preprint. Discussion started: 6 February 2025

The input datasets can be found at NSIDC (ice motion: https://nsidc.org/data/nsidc-0116/versions/4; ice extent: https://nsidc.org/data/nsidc-0051/versions/2) and AVISO website (dynamic topography: https://www.aviso.altimetry.fr/en/data/products/sea-surface-height-products/regional/arctic-ocean-sea-level-heights.html). ITP-V data used in this work are retrieved from the WHOI website at https://www2.whoi.edu/site/itp/. CPOM-DOT/geostrophic currents data are provided by the Centre for Polar Observation and Modelling, University College London (https://www.cpom.ucl.ac.uk/dynamic_topography).

6 Conclusions

This work presents a daily, 25 km resolution dataset of satellite-derived ocean-surface stress for the Arctic (2011-2018) and Southern Oceans (2013-2018). The dataset provides detailed daily maps of τ_o across polar regions north of 60°N and south of 50°S. This dataset achieves finer spatial and temporal resolution, enabling more precise analysis of short-term air-sea interactions and regional Ekman dynamics. In both the Arctic and Antarctic, it captures short-term and sharp transition between Ekman upwelling in ice-free regions and downwelling in ice-covered areas.

Uncertainty in the derived ocean-surface stress fields arises primarily from two sources. The first is the spatial filter applied to the SSH datasets, which reduces small scale variability and enhances consistency between the sea level fields. The second source of uncertainty is related to the ice-water drag coefficient, which is poorly observed and can vary significantly between order of 10^{-3} and 10^{-2}. These factors result in a median uncertainty of approximately 20% in the Arctic and about 40% in the Southern Ocean.

The derived Ekman velocity is used to validate against ITP data from the Arctic's Canada Basin. Satellite-derived surface velocity, which combine Ekman and geostrophic components, capture over 50% of the observed variation in surface velocity. Correlation coefficients range from 0.6 to 0.8 on monthly and longer timescales, indicating moderate to strong agreement. It is important to consider the complex dynamics of the Arctic Ocean when interpreting these statistics. In addition to Ekman and geostrophic velocity (Regan et al., 2019), processes such as shallow eddy activity (Timmermans et al., 2008; Kenigson et al., 2021; Meneghello et al., 2021), turbulent mixing (Guthrie et al., 2013; Kawaguchi et al., 2014, 2019), and internal waves (Kawaguchi et al., 2016; Zhao et al., 2016) also contribute to the observed variability. Many of these processes remain challenging to observe and parameterize.

Future updates will focus on two primary areas. First, once the OAFlux ice mask is corrected, we will incorporate 2021 data into the dataset to extend its temporal coverage. Second, the availability of reliable surface height products for the polar region will further enhance data accuracy. While awaiting these advancements, we will assess the potential impacts of transitioning to reanalysis data on our results. Additionally, future research will address key processes that remain underrepresented, such as variable Ekman depth and mesoscale turbulence, to refine the depiction of polar ocean dynamics. Incorporating these factors will improve the ability to capture localized features critical for understanding air-ice-ocean interactions.

https://doi.org/10.5194/essd-2025-14
Preprint. Discussion started: 6 February 2025

Author contributions

CL: conceptualization, data curation, formal analysis, methodology, software, visualization, writing – original draft preparation, writing – review and editing. LY: conceptualization, project administration, supervision, validation, writing – review and editing.

Competing interests

The contact author has declared that none of the authors has any competing interests.

Finance Support

This project is supported by NASA under grant no. 80NSSC23K0981.

References

Anderson, M. R.: The onset of spring melt in first-year ice regions of the Arctic as determined from scanning multichannel microwave radiometer data for 1979 and 1980. Journal of Geophysical Research: Oceans, 92(C12), 13153-13163, 1987.

Ardyna, M., & Arrigo, K. R.: Phytoplankton dynamics in a changing Arctic Ocean. Nature Climate Change, 10(10), 892-903, 2020.

Armitage, T. W., Bacon, S., Ridout, A. L., Thomas, S. F., Aksenov, Y., & Wingham, D. J.: Arctic sea surface height variability and change from satellite radar altimetry and GRACE, 2003–2014. Journal of Geophysical Research: Oceans, 121(6), 4303-4322, 2016.

Armitage, T. W. K., Bacon, S., Ridout, A. L., Petty, A. A., Wolbach, S., and Tsamados, M.: Arctic Ocean surface geostrophic circulation 2003–2014, The Cryosphere, 11, 1767– 1780, https://doi.org/10.5194/tc-11-1767-2017, 2017.

Auger M, Prandi P, Sallée J B. Southern ocean sea level anomaly in the sea ice-covered sector from multimission satellite observations. Scientific Data, 9(1): 70, 2022.

Campbell EC, Wilson EA, Moore GK, Riser SC, Brayton CE, Mazloff MR, Talley LD. Antarctic offshore polynyas linked to Southern Hemisphere climate anomalies. Nature. 570(7761):319-25, 2019.

Cassianides, A., Lique, C., Tréguier, A. M., Meneghello, G., & De Marez, C.: Observed Spatio-Temporal Variability of the Eddy-Sea Ice Interactions in the Arctic Basin. Journal of Geophysical Research: Oceans, 128(6), e2022JC019469, 2023.

Cavalieri, D. J., C. L. Parkinson, P. Gloersen, and H. J. Zwally: Sea ice concentrations from Nimbus-7 SMMR and DMSP SSM/I-SSMIS passive microwave data, version 1. NSIDC, https://doi.org/10.5067/ 8GQ8LZQVL0VL., 1996

Cole, S. T., & Stadler, J.: Deepening of the winter mixed layer in the Canada basin, Arctic Ocean over 2006–2017. Journal of Geophysical Research: Oceans, 124(7), 4618-4630, 2019.

Cole, S. T., M.-L. Timmermans, J. M. Toole, R. A. Krishfield, and F. T. Thwaites: Ekman veering, internal waves, and turbulence observed under Arctic sea ice. J. Phys. Oceanogr., 44, 1306–1328, https://doi.org/10.1175/JPO-D-12-0191.1, 2014.

DiGirolamo, N. E., C. L. Parkinson, D. J. Cavalieri, P. Gloersen, and H. J. Zwally.: updated yearly. Sea Ice Concentrations from Nimbus-7 SMMR and DMSP SSM/I-SSMIS Passive Microwave Data, Version 2. Boulder, Colorado USA. NASA National Snow and Ice Data Center Distributed Active Archive Center. https://doi.org/10.5067/MPYG15WAA4WX, 2022.

Eayrs, C., Holland, D. M., Francis, D., Wagner, T. J. W., Kumar, R., & Li, X. Understanding the seasonal cycle of Antarctic sea ice extent in the context of longer-term variability. Reviews of Geophysics. 57, 1037–1064. https://doi.org/10.1029/2018RG000631, 2019

Fairall, C. W., Bradley, E. F., Hare, J. E., Grachev, A. A., & Edson, J. B.: Bulk parameterization of air–sea fluxes: Updates and verification for the COARE algorithm. Journal of climate, 16(4), 571-591, 2003.

Guest, P. S., & Davidson, K. L.: The effect of observed ice conditions on the drag coefficient in the summer East Greenland Sea marginal ice zone. Journal of Geophysical Research: Oceans, 92(C7), 6943-6954, 1987.

Guest, P. S., and Davidson, K. L.: The aerodynamic roughness of different types of sea ice, J. Geophys. Res., 96(C3), 4709–4721, 1991.

Guthrie, J. D., Morison, J. H., & Fer, I.: Revisiting internal waves and mixing in the Arctic Ocean. Journal of Geophysical Research: Oceans, 118(8), 3966-3977, 2013.

Kalnay, E., Kanamitsu, M., Kistler, R., Collins, W., Deaven, D., Gandin, L., Iredell, M., Saha, S., White, G., Woollen, J., and Zhu, Y.: The NCEP/NCAR 40-year reanalysis project, B. Am. Meteorol. Soc., 77, 437–471, https://doi.org/10.1175/1520-0477(1996)077<0437:TNYRP>2.0.CO;2, 1996.

Kaplan, J. O., & New, M.: Arctic climate change with a 2∘ C global warming: Timing, climate patterns and vegetation change. Climatic change, 79, 213-241, 2006.

Kawaguchi, Y., Hoppmann, M., Shirasawa, K. et al. Dependency of the drag coefficient on boundary layer stability beneath drifting sea ice in the central Arctic Ocean. Sci Rep 14, 15446, 2024

Kawaguchi, Y., Itoh, M., Fukamachi, Y., Mori,ya, E., Onodera, J., Kikuchi, T., & Harada, N.: Year-round observations of sea-ice drift and near-inertial internal waves in the Northwind Abyssal Plain, Arctic Ocean. Polar Science, 21, 212-223, 2019.

Kawaguchi, Y., Kikuchi, T., & Inoue, R.: Vertical heat transfer based on direct microstructure measurements in the ice-free Pacific-side Arctic Ocean: the role and impact of the Pacific water intrusion. Journal of oceanography, 70, 343-353, 2014.

Kawaguchi, Y., Nishino, S., Inoue, J., Maeno, K., Takeda, H., & Oshima, K.: Enhanced diapycnal mixing due to near-inertial internal waves propagating through an anticyclonic eddy in the ice-free Chukchi Plateau. Journal of Physical Oceanography, 46(8), 2457-2481, 2016.

Kenigson, J.S., Gelderloos, R. and Manucharyan, G.E., Vertical structure of the Beaufort Gyre halocline and the crucial role of the depth-dependent eddy diffusivity. Journal of Physical Oceanography, 51(3), pp.845-860. 2021.

Krishfield, R., Toole, J., Proshutinsky, A., & Timmermans, M. L.: Automated ice-tethered profilers for seawater observations under pack ice in all seasons. Journal of Atmospheric and Oceanic Technology, 25(11), 2091-2105, 2008.

https://doi.org/10.5194/essd-2025-14
Preprint. Discussion started: 6 February 2025

Kwok, R.: Arctic sea ice thickness, volume, and multiyear ice coverage: losses and coupled variability (1958–2018), En- viron. Res. Lett., 13, 105005, https://doi.org/10.1088/1748- 9326/aae3ec, 2018.

Lefebvre, W., Goosse, H., Timmermann, R. and Fichefet, T., Influence of the Southern Annular Mode on the sea ice–ocean system. Journal of Geophysical Research: Oceans, 109(C9). 2004.

Liu, C., and Yu, L.: Arctic Ocean-Surface Stress Analysis, 2011-2018, Zenodo [data set], https://doi.org/10.5281/zenodo.12735199, 2024.

Lüpkes, C., & Birnbaum, G.: Surface drag in the Arctic marginal sea-ice zone: A comparison of different parameterisation concepts. Boundary-layer meteorology, 117, 179-211, 2005.

Lüpkes, C., Gryanik, V. M., Hartmann, J., & Andreas, E. L.: A parametrization, based on sea ice morphology, of the neutral atmospheric drag coefficients for weather prediction and climate models. Journal of Geophysical Research: Atmospheres, 117(D13), 2012.

Ma, B., M. Steele, and C. M. Lee: Ekman circulation in the Arctic Ocean: Beyond the Beaufort Gyre. J. Geophys. Res. Oceans, 122, 3358–3374, https://doi.org/10.1002/2016JC012624, 2017.

Martin, T., Steele, M. and Zhang, J., Seasonality and long-term trend of Arctic Ocean surface stress in a model. Journal of Geophysical Research: Oceans, 119(3), pp.1723-1738. 2014.

McPhee, M. G. Air-ice-ocean interaction—Turbulent ocean boundary layer exchange processes (Springer, New York, 2008).

McPhee, M. G.: Intensification of geostrophic currents in the Canada Basin, Arctic Ocean. J. Climate, 26, 3130–3138, https:// doi.org/10.1175/JCLI-D-12-00289.1, 2013.

Meehl, G. A. et al. Sustained ocean changes contributed to sudden Antarctic sea ice retreat in late 2016. Nat. Commun. 10, 14, 2019.

Meier, W. N. et al.: NOAA Arctic Report Card 2023: Sea Ice. https://doi.org/10.25923/f5t4-b865, 2023.

Meneghello, G., J. Marshall, S. T. Cole, and M.-L. Timmermans: Observational inferences of lateral eddy diffusivity in the halocline of the Beaufort Gyre. Geophys. Res. Lett., 44, 12 331–12 338, https://doi.org/10.1002/2017GL075126, 2017.

Meneghello, G., Marshall, J., Lique, C., Isachsen, P.E., Doddridge, E., Campin, J.M., Regan, H. and Talandier, C., Genesis and decay of mesoscale baroclinic eddies in the seasonally ice-covered interior Arctic Ocean. Journal of Physical Oceanography, 51(1), pp.115-129. 2021.

Meneghello, G., Marshall, J., Timmermans, M. L., & Scott, J.: Observations of seasonal upwelling and downwelling in the Beaufort Sea mediated by sea ice. Journal of Physical Oceanography, 48(4), 795-805, 2018.

Meredith, M., Sommerkorn, M., Cassotta, S., Derksen, C., Ekaykin, A., Hollowed, A., Kofinas, G., Mackintosh, A., Melbourne-Thomas, J., Muelbert, M., Ottersen, G., Pritchard, H., and Schuur, E.: Polar Regions, Cahp. 3, IPCC's Special Report on the Ocean and Cryosphere in a Changing Climate, 2019.

Moore, G.W.K., Steele, M., Schweiger, A.J., Zhang, J. and Laidre, K.L.. Thick and old sea ice in the Beaufort Sea during summer 2020/21 was associated with enhanced transport. *Communications Earth & Environment*, *3*(1), p.198, 2022.

https://doi.org/10.5194/essd-2025-14
Preprint. Discussion started: 6 February 2025

Overland, J. E.: Atmospheric boundary layer structure and drag coefficients over sea ice, J. Geophys. Res., 90(C5), 9029–9049, 1985.

Overland, J., Dunlea, E., Box, J. E., Corell, R., and co-authors: The urgency of Arctic change. Polar Science, 21, 6-13,. 2019.

Park, H.S., Stewart, A.L. and Son, J.H., Dynamic and thermodynamic impacts of the winter Arctic Oscillation on summer sea ice extent. Journal of Climate, 31(4), pp.1483-1497. 2018.

Parkinson, C. L.: A 40-y record reveals gradual Antarctic sea ice increases followed by decreases at rates far exceeding the rates seen in the Arctic. Proceedings of the National Academy of Sciences, 116(29), 14414-14423, 2019.

Polvani, L. M. & Smith, K. L. Can natural variability explain observed Antarctic sea ice trends? New modeling evidence from CMIP5. Geophys. Res. Lett. 40, 3195–3199 2013.

Polyakov, I. V., Pnyushkov, A. V., Alkire, M. B., and co-authors: Greater role for Atlantic inflows on sea-ice loss in the Eurasian Basin of the Arctic Ocean, Science, 356, 285–291, https://doi.org/10.1126/science.aai8204, 2017.

Prandi, P., Poisson, J.-C., Faugère, Y., Guillot, A., and Dibarboure, G.: Arctic sea surface height maps from multi-altimeter combination, Earth Syst. Sci. Data, 13, 5469–5482, https://doi.org/10.5194/essd-13-5469-2021, 2021

Proshutinsky, A., Dukhovskoy, D., Timmermans, M. L., Krishfield, R., and Bamber, J. L.: Arctic circulation regimes, Philos. T. R. Soc. A, 373, 20140160, https://doi.org/10.1098/rsta.2014.0160, 2015.

Purich, A. and Doddridge, E.W., Record low Antarctic sea ice coverage indicates a new sea ice state. Communications Earth & Environment, 4(1), p.314. 2023.

Ramadhan A, Marshall J, Meneghello G, et al. Observations of upwelling and downwelling around Antarctica mediated by sea ice. Frontiers in Marine Science, 9: 864808, 2022.

Regan, H. C., Lique, C., and Armitage, T. W. K.: The Beaufort Gyre Extent, Shape, and Location Between 2003 and 2014 From Satellite Observations, J. Geophys. Res.-Oceans, 124, 844–862, https://doi.org/10.1029/2018JC014379, 2019.

Regan, H., Lique, C., Talandier, C., and Meneghello, G.: Response of total and eddy kinetic energy to the recent spin up of the Beaufort Gyre, J. Phys. Oceanogr., 50, 575–594, https://doi.org/10.1175/JPO-D-19-0234.1, 2020.

Rigor, I.G., Wallace, J.M. and Colony, R.L., 2002. Response of sea ice to the Arctic Oscillation. Journal of Climate, 15(18), pp.2648-2663.

Sévellec, F., Fedorov, A. V., & Liu, W.: Arctic sea-ice decline weakens the Atlantic meridional overturning circulation. Nature Climate Change, 7(8), 604-610, 2017.

Solomon, A., Heuzé, C., Rabe, B., Bacon, S., Bertino, L., Heimbach, P., ... & Tang, H.: Freshwater in the arctic ocean 2010–2019. Ocean Science, 17(4), 1081-1102, 2021.

Stammerjohn, S., Massom, R. A., Rind, D. & Martinson, D. G. Regions of rapid sea ice change: an inter-hemispheric seasonal comparison. Geophys. Res. Lett. 39, L06501 (2012).

Stroeve, J., & Notz, D.: Changing state of Arctic sea ice across all seasons. Environmental Research Letters, 13(10), 103001, 2018.

https://doi.org/10.5194/essd-2025-14
Preprint. Discussion started: 6 February 2025

Sumata H, Lavergne T, Girard-Ardhuin F, Kimura N, Tschudi MA, Kauker F, Karcher M, Gerdes R. An intercomparison of Arctic ice drift products to deduce uncertainty estimates. Journal of Geophysical Research: Oceans. 2014 Aug;119(8):4887-921.

Thorndike, A.S. and Colony, R., Sea ice motion in response to geostrophic winds. Journal of Geophysical Research: Oceans, 87(C8), pp.5845-5852. 1982.

Timmermans, M. L., & Marshall, J.: Understanding Arctic Ocean circulation: A review of ocean dynamics in a changing climate. Journal of Geophysical Research: Oceans, 125(4), e2018JC014378, 2020.

Timmermans, M. L., Toole, J., Proshutinsky, A., Krishfield, R., & Plueddemann, A.: Eddies in the Canada Basin, Arctic Ocean, observed from ice-tethered profilers. Journal of Physical Oceanography, 38(1), 133-145, 2008.

Timmermans, M.-L., Ladd, C., and Wood, K.: Sea surface temperature, Arctic Report Card, available at: https://arctic.noaa.gov/Report-Card/Report-Card-2017/ArtMID/ 7798/ArticleID/698/Sea-Surface-Temperature, 2017.

Toole, J. M., R. A. Krishfield, M.-L. Timmermans, and A. Proshutinsky: The ice-tethered profiler: Argo of the Arctic. Oceanography, 24 (3), 126–135, https://doi.org/10.5670/oceanog.2011.64, 2011.

Tschudi, M. A., Meier, W. N., & Stewart, J. S.: An enhancement to sea ice motion and age products at the National Snow and Ice Data Center (NSIDC). The Cryosphere, 14(5), 1519-1536, 2020.

Tschudi, M., Meier, W. N., Stewart, J. S., Fowler, C., and Maslanik, J.: Polar Pathfinder Daily 25 km EASE-Grid Sea Ice Motion Vectors, Version 4, Boulder, CA, USA, NASA National Snow and Ice Data Center Distributed Active Archive Center, https://doi.org/10.5067/INAWUWO7QH7B, 2019.

Turner J, Holmes C, Caton Harrison T, Phillips T, Jena B, Reeves-Francois T, Fogt R, Thomas ER, Bajish CC. Record low Antarctic sea ice cover in February 2022. Geophysical Research Letters. 2022 Jun 28;49(12):e2022GL098904.

Wang X, Chen R, Li C, Chen Z, Hui F, Cheng X. An intercomparison of satellite derived Arctic sea ice motion products. Remote Sensing. 2022 Mar 4;14(5):1261.

Wu, Y., Wang, Z., Liu, C. and Yan, L., Impacts of Ice-Ocean Stress on the Subpolar Southern Ocean: Role of the Ocean Surface Current. Advances in Atmospheric Sciences, 41(2), pp.293-309. 2024.

Yang, J.: Seasonal and interannual variability of downwelling in the Beaufort Sea. J. Geophys. Res., 114, C00A14, https:// doi.org/10.1029/2008JC005084, 2009.

Yang, J.: The seasonal variability of the Arctic Ocean Ekman transport and its role in the mixed layer heat and salt fluxes. J. Climate, 19, 5366–5387, https://doi.org/10.1175/ JCLI3892.1, 2006.

Yu, L., & Jin, X.: Confidence and sensitivity study of the OAFlux multisensor synthesis of the global ocean surface vector wind from 1987 onward. Journal of Geophysical Research: Oceans, 119(10), 6842-6862, 2014b.

Yu, L., & Jin, X.: Insights on the OAFlux ocean surface vector wind analysis merged from scatterometers and passive microwave radiometers (1987 onward). Journal of Geophysical Research: Oceans, 119(8), 5244-5269, 2014a.

Yu, L., Bingham, F. M., Lee, T., Dinnat, E. P., Fournier, S., Melnichenko, O., Tang, W., Yueh, S. H.: Revisiting the global patterns of seasonal cycle in sea surface salinity. J. Geophys. Res. Oceans, 126, e2020JC016789. https://doi.org/10.1029/2020JC016789, 2021.

Yu, L.: Global air–sea fluxes of heat, fresh water, and momentum: Energy budget closure and unanswered questions. Annual Review of Marine Science, 11(1), 227–248. https://doi.org/10.1146/annurev-marine-010816-060704, 2019.

Zhao, M., Timmermans, M.-L., Cole, S., Krishfield, R., and Toole, J.: Evolution of the eddy field in the Arctic Ocean's Canada Basin, 2005–2015, Geophys. Res. Lett., 43, 8106–8114, https://doi.org/10.1002/2016GL069671, 2016.